Commun Nonlinear Sci Numer Simulat 162 (2026) 110319

Contents lists available at ScienceDirect

Communications in Nonlinear Science and Numerical Simulation

journal homepage: www.elsevier.com/locate/cnsns

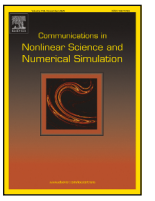

Research paper

A fully coupled FBSDE framework for optimal orbit steering near an Arneodo-Coullet-Tresser spiral attractor

Dong Feng

Faculty of Civil Engineering, RWTH Aachen University, Mies-van-der-Rohe-Straße 1, Aachen, 52074, Germany

ARTICLE INFO

Keywords:
Arneodo-Coullet-Tresser attractor
Fully coupled FBSDE
Stochastic maximum principle
Chaotic orbit steering
Spiral chaos
Stochastic tracking

ABSTRACT

This paper develops a fully coupled forward-backward stochastic differential equation (FBSDE) framework for optimal orbit steering near a spiral attractor generated by an Arneodo-Coullet-Tresser-type chaotic oscillator. The central objective is to preserve the intrinsic orbital geometry of the attractor while reducing stochastic deviations from a prescribed reference orbit segment. To achieve this goal, a stochastic tracking problem is formulated for a noisy controlled ACT system, and the corresponding stochastic maximum principle yields a nonlinear fully coupled FBSDE in which the third backward component enters the active chaotic channel through the optimal feedback law. The resulting model establishes a direct link between spiral chaotic dynamics, stochastic optimal control, and adjoint backward propagation. A compact tensor formulation is provided, together with a variational derivation, a local solvability discussion under structured assumptions, and a decoupling-field interpretation. The framework offers a mathematically coherent and comparatively underexplored route for investigating stochastic orbit steering, random attractor neighborhoods, and control-energy allocation in a spiral chaotic environment.

1. Introduction

Nonlinear chaotic oscillators subject to uncertainty arise in a wide variety of scientific contexts, including fluid transport [1,2], nonlinear circuits [3,4], mechanical vibration [5–7], and stochastic signal propagation [8–10]. In such systems, deterministic instability is often intertwined with external fluctuations [11], parametric uncertainty [12], and incomplete information about forcing mechanisms [13]. As a consequence, a purely deterministic description may fail to capture the effective transport properties of trajectories over long time intervals. This is particularly true when the underlying dynamics possess strong sensitivity to initial data and repeated stretching and folding mechanisms [14–16]. In these settings, stochastic differential equations (SDEs) provide a natural mathematical framework for incorporating random perturbations into nonlinear dynamical models while preserving the essential geometric structure of the original deterministic flow [17–19]. At the same time, chaotic attractors remain central objects of interest, since they encode the long-time organization of trajectories and reflect the qualitative mechanisms responsible for complex oscillatory behavior [20–22].

Among the many classes of three-dimensional chaotic systems, the Arneodo-Coullet-Tresser (ACT) family [23–25] occupies a distinctive position because of its ability to generate spiral-type attractors with rich reinjection geometry. Compared with more frequently studied Lorenz-type systems [26–28], ACT dynamics exhibit a different form of orbital organization, in which trajectories rotate around a core region before undergoing global return. This spiral structure is not only visually characteristic, but also dynamically meaningful, since it provides a useful setting for studying nontrivial transport near non-equilibrium invariant sets. When

E-mail address: dong.feng@rwth-aachen.de

https://doi.org/10.1016/j.cnsns.2026.110319
Received 14 March 2026; Received in revised form 25 April 2026; Accepted 6 June 2026
Available online 8 June 2026

Table 1
Representative literature related to BSDE/FBSDE applications and the positioning of the present study.

Line of work	Representative literature	Main objective	Difference from the present study
Foundational BSDE/FBSDE theory	Pardoux and Peng [31]; Ma and Yong [46]	Existence, uniqueness, and general FBSDE methodology	Focuses on general theory rather than chaotic orbit control
BSDE/FBSDE in stochastic control and games	Hamadène and Lepeltier [47]	Optimal control and stochastic differential games	Does not address spiral chaotic attractors or geometry-preserving orbit steering
BSDE applications in finance	El Karoui, Peng, and Quenez [30]	Pricing, recursive utility, and financial decision problems	Application domain is finance rather than nonlinear chaotic dynamics
Forward-backward stochastic methods in filtering	Archibald et al. [48]	State estimation and data assimilation under uncertainty	Uses backward or forward-backward stochastic systems for filtering, not for chaotic orbit tracking control
Mainstream chaotic control literature	Dykman et al. [11]; Fotsin and Daafouz [12]; Tegnitsap et al. [3]	Synchronization, suppression, or forcing-based regulation of chaotic motion	Typically not formulated as a fully coupled FBSDE with backward adjoint orbit steering
Present study	This work	Stochastic optimal orbit steering near an ACT spiral attractor	Uses a fully coupled FBSDE to preserve orbit geometry while reducing stochastic deviation

stochastic forcing is introduced, the deterministic attractor is no longer represented by a single invariant object in the classical sense [29]. Instead, one observes a random neighborhood shaped by the deterministic skeleton and continuously deformed by diffusion. Such a viewpoint is relevant in applications where noise cannot be neglected and where one wishes to understand how random perturbations alter orbit geometry, recurrence patterns, and the energetic cost of maintaining coherent motion near a chaotic set.

In parallel with the development of stochastic dynamics, forward-backward stochastic differential equations (FBSDEs) [30,31] have become one of the most powerful tools in stochastic control [32,33], nonlinear filtering [34,35], and probabilistic representations of nonlinear partial differential equations [36–38]. In particular, coupled FBSDEs provide a natural mathematical language for problems in which the future cost of the system influences present optimal decisions through a backward adjoint variable [39–41]. Nevertheless, the existing interaction between FBSDE theory and chaotic attractor control remains relatively limited. A large part of the available literature focuses either on equilibrium stabilization [42], synchronization [43], or control of more standard benchmark systems [44]. Even when stochastic control is considered, the objective is often to suppress chaotic motion rather than to preserve its intrinsic orbital structure [45]. This creates a clear limitation in the current literature. For many chaotic systems, especially those with spiral attractor geometry, forcing the state to a fixed point does not reflect the true dynamical objective. What is often needed instead is a control design that respects the nontrivial orbit structure of the attractor while reducing random deviations from a desirable trajectory segment embedded in that attractor.

In this context, it is important to distinguish the broad development of BSDE and FBSDE theory from their much more limited use in chaotic orbit regulation. Existing BSDE and FBSDE studies are mainly concentrated in stochastic control, filtering, finance, and probabilistic representations of nonlinear partial differential equations, where the main concern is the characterization of adjoint processes, value functions, or estimation mechanisms. By contrast, the mainstream literature on chaotic systems has focused more often on stabilization, synchronization, or suppression of chaotic oscillations. Comparatively fewer studies have formulated chaotic orbit regulation itself within a fully coupled forward-backward stochastic framework, especially for spiral attractors with reference-orbit tracking objectives. For clarity, Table 1 summarizes the positioning of the present work relative to several representative research directions.

Motivated by this observation, the present paper develops a fully coupled forward-backward stochastic framework for optimal orbit steering near an ACT spiral attractor. Rather than stabilizing the noisy system to an equilibrium, the proposed model tracks a deterministic reference orbit segment extracted from the ACT attractor itself. This formulation leads naturally to a stochastic optimal control problem with quadratic tracking and control penalties, from which a nonlinear fully coupled FBSDE is derived by means of the stochastic maximum principle. In the resulting system, the third backward component enters the active chaotic channel through the optimal feedback law, thereby establishing a direct dynamical coupling between the forward spiral motion and the backward adjoint field. The paper presents the model in componentwise form and compact tensor form, provides a variational derivation, discusses local well-posedness under structured assumptions, and gives a decoupling-field interpretation together with a time-discrete approximation framework.

2. Stochastic orbit steering for the ACT system

Let $t \in [0,T]$, where $T > 0$ is a fixed time horizon. Let $\mathbf{X}_t \in \mathbb{R}^3$ denote the forward state vector at time t. The notation $\mathbb{R}^3$ denotes the three-dimensional Euclidean space. Let $U_t \in \mathbb{R}$ denote the scalar control input. Let W_t be a standard one-dimensional Brownian motion defined on a filtered probability space $\left(\Omega, \mathcal{F}, \{\mathcal{F}_t\}_{t\in[0,T]}, \mathbb{P}\right)$, where Ω is the sample space, $\mathcal{F}$ is the σ-algebra, $\{\mathcal{F}_t\}$ is the filtration representing the available information up to time t, and $\mathbb{P}$ is the probability measure.

We start from a deterministic ACT oscillator written as:

$$\dot{x}_1(t) = x_2(t),$$
$$\dot{x}_2(t) = x_3(t),$$

$$\dot{x}_3(t) = ax_1(t) - bx_2(t) - cx_3(t) - dx_1(t)^2, \tag{1}$$

where $x_1(t)$, $x_2(t)$, $x_3(t) \in \mathbb{R}$ are scalar state components. The parameters a, b, c, $d \in \mathbb{R}$ describe, respectively, the linear excitation in the first channel, the linear coupling-damping contribution from the second channel, the direct damping in the third channel, and the nonlinear quadratic effect in the first state variable.

Introducing the state vector:

$$\mathbf{x}(t) = \begin{bmatrix} x_1(t) \\ x_2(t) \\ x_3(t) \end{bmatrix}, \tag{2}$$

the deterministic dynamics can be written compactly as:

$$\mathbf{f}_0(\mathbf{x}) = \dot{\mathbf{x}}(t) = \begin{bmatrix} x_2 \\ x_3 \\ ax_1 - bx_2 - cx_3 - dx_1^2 \end{bmatrix}, \tag{3}$$

where $\mathbf{f}_0 : \mathbb{R}^3 \to \mathbb{R}^3$ is the nonlinear drift field.

To account for control, let $\mathbf{e}_3 = (0, 0, 1)^T \in \mathbb{R}^3$ denote the third canonical basis vector. The controlled deterministic system becomes:

$$\dot{\mathbf{x}}(t) = \mathbf{f}_0(\mathbf{x}(t)) + \mathbf{e}_3 U_t. \tag{4}$$

Then, we introduce stochastic perturbations through the following Itô equation [49]:

$$d\mathbf{X}_t = \mathbf{f}\left(\mathbf{X}_t, U_t\right)dt + \mathbf{\Sigma} d\mathbf{W}_t, \tag{5}$$

where $\mathbf{f} : \mathbb{R}^3 \times \mathbb{R} \to \mathbb{R}^3$ is the controlled drift:

$$\mathbf{f}(\mathbf{x}, u) = \begin{bmatrix} x_2 \\ x_3 \\ ax_1 - bx_2 - cx_3 - dx_1^2 + u \end{bmatrix}, \tag{6}$$

and $\mathbf{\Sigma} \in \mathbb{R}^{3\times 1}$ is the diffusion tensor. In the present setting, only the third channel is directly perturbed, and therefore:

$$\mathbf{\Sigma} = \begin{bmatrix} 0 \\ 0 \\ \sigma \end{bmatrix}, \tag{7}$$

where $\sigma > 0$ denotes the diffusion intensity.

In the present model, the diffusion term is deliberately introduced only through the third channel. From the structural viewpoint (see Eq. (6)), the ACT dynamics are driven most directly through the third equation, where the nonlinear restoring and excitation effects are concentrated, so perturbing this channel already propagates randomness to the full three-dimensional state through the intrinsic coupling $x_1 \to x_2 \to x_3$. From the modeling viewpoint, this single-channel additive noise provides a minimal stochastic setting that preserves analytical tractability and makes the forward-backward coupling easier to interpret. Accordingly, the single-channel additive noise is treated as a reduced but dynamically meaningful baseline assumption rather than as the most general noise model. In more elaborate settings, one may certainly consider multi-channel or state-dependent diffusion terms, but the present formulation is sufficient for studying how stochastic perturbations interact with orbit steering near the ACT spiral attractor.

The forward stochastic dynamics can now be written componentwise as:

$$\begin{aligned} dX_{1,t} &= X_{2,t}dt, \\ dX_{2,t} &= X_{3,t}dt, \\ dX_{3,t} &= \left(aX_{1,t} - bX_{2,t} - cX_{3,t} - dX_{1,t}^2 + U_t\right)dt + \sigma dW_t. \end{aligned} \tag{8}$$

The random initial state is denoted by $\mathbf{X}_0 = \boldsymbol{\xi}$, where $\boldsymbol{\xi}$ is an $\mathcal{F}_0$-measurable random vector satisfying the square-integrability condition $\mathbb{E}\|\boldsymbol{\xi}\|^2 < \infty$. The Euclidean norm is denoted by $\|\cdot\|$. For any symmetric positive semidefinite tensor $\mathbf{M} \in \mathbb{R}^{3\times 3}$, the weighted quadratic form is defined by:

$$\|\mathbf{x}\|_{\mathbf{M}}^2 = \mathbf{x}^T \mathbf{M} \mathbf{x}. \tag{9}$$

A deterministic reference orbit segment is extracted from the uncontrolled ACT attractor and denoted by $\bar{\mathbf{x}} : [0, T] \to \mathbb{R}^3$. It satisfies:

$$\dot{\bar{\mathbf{x}}}(t) = \mathbf{f}_0\left(\bar{\mathbf{x}}(t)\right). \tag{10}$$

In components:

$$\begin{aligned} \dot{\bar{x}}_1(t) &= \bar{x}_2(t), \\ \dot{\bar{x}}_2(t) &= \bar{x}_3(t), \\ \dot{\bar{x}}_3(t) &= a\bar{x}_1(t) - b\bar{x}_2(t) - c\bar{x}_3(t) - d\bar{x}_1(t)^2. \end{aligned} \tag{11}$$

This reference orbit is central to the entire construction. Instead of forcing the noisy system toward a point equilibrium, the controller is asked to keep the stochastic state near this moving target. Such a design preserves the geometric identity of the spiral chaotic motion while still suppressing excessive random deviation.

Let $\mathbf{Q} \in \mathbb{R}^{3\times3}$ and $\mathbf{G} \in \mathbb{R}^{3\times3}$ be symmetric positive semidefinite tensors representing running and terminal tracking weights, respectively. Let $r > 0$ denote the scalar control penalty. The stochastic cost functional is defined by:

$$J(U) = \mathbb{E}\left[\int_0^T \left(\|\mathbf{X}_t - \bar{\mathbf{x}}(t)\|_{\mathbf{Q}}^2 + rU_t^2\right)dt + \|\mathbf{X}_T - \bar{\mathbf{x}}(T)\|_{\mathbf{G}}^2\right]. \tag{12}$$

The admissible control class is:

$$\mathcal{U} = \left\{ U : [0,T]\times\Omega \to \mathbb{R} \,\middle|\, U_t \text{ is } \mathcal{F}_t - \text{adapted and } \mathbb{E}\int_0^T U_t^2 dt < \infty \right\}. \tag{13}$$

Then, the stochastic optimal control problem is $\inf_{U\in\mathcal{U}} J(U)$ subject to Eq. (5) with $\mathbf{X}_0 = \boldsymbol{\xi}$. To describe deviations from the target orbit, define the tracking error:

$$\mathbf{E}_t = \mathbf{X}_t - \bar{\mathbf{x}}(t). \tag{14}$$

Then, we have:

$$d\mathbf{E}_t = \left(\mathbf{f}(\mathbf{X}_t, U_t) - \mathbf{f}_0(\bar{\mathbf{x}}(t))\right)dt + \boldsymbol{\Sigma} dW_t. \tag{15}$$

Its components satisfy:

$$\begin{aligned} dE_{1,t} &= E_{2,t}dt, \\ dE_{2,t} &= E_{3,t}dt, \\ dE_{3,t} &= \left(aE_{1,t} - bE_{2,t} - cE_{3,t} - d\left(X_{1,t}^2 - \bar{x}_1(t)^2\right) + U_t\right)dt + \sigma dW_t. \end{aligned} \tag{16}$$

Using:

$$X_{1,t}^2 - \bar{x}_1(t)^2 = \left(X_{1,t} - \bar{x}_1(t)\right)\left(X_{1,t} + \bar{x}_1(t)\right) = E_{1,t}\left(X_{1,t} + \bar{x}_1(t)\right), \tag{17}$$

the third error equation can also be written as:

$$dE_{3,t} = \left(aE_{1,t} - bE_{2,t} - cE_{3,t} - dE_{1,t}\left(X_{1,t} + \bar{x}_1(t)\right) + U_t\right)dt + \sigma dW_t. \tag{18}$$

The objective functional becomes:

$$J(U) = \mathbb{E}\left[\int_0^T \left(\mathbf{E}_t^T\mathbf{Q}\mathbf{E}_t + rU_t^2\right)dt + \mathbf{E}_T^T\mathbf{G}\mathbf{E}_T\right]. \tag{19}$$

This formulation reveals the essential structure of the problem. The tracking objective is quadratic, the control cost is quadratic, the forward drift is nonlinear because of the ACT term $-dX_{1,t}^2$, and the random forcing acts only in the third channel. These ingredients are exactly what make the resulting backward adjoint equation both analytically rich and dynamically meaningful.

3. Hamiltonian structure and the fully coupled FBSDE

We now derive the optimality system by means of the stochastic maximum principle. Let $\mathbf{Y}_t \in \mathbb{R}^3$ denote the adjoint process and $\mathbf{Z}_t \in \mathbb{R}^{3\times1}$ denote the backward martingale coefficient. The stochastic Hamiltonian is defined by:

$$\mathcal{H}(t,\mathbf{x},u,\mathbf{y},\mathbf{z}) = \left(\mathbf{x} - \bar{\mathbf{x}}(t)\right)^T\mathbf{Q}\left(\mathbf{x} - \bar{\mathbf{x}}(t)\right) + ru^2 + \mathbf{y}^T\mathbf{f}(\mathbf{x},u) + \mathbf{z}^T\boldsymbol{\Sigma}. \tag{20}$$

Expanding the drift contribution gives:

$$\mathbf{y}^T\mathbf{f}(\mathbf{x},u) = y_1x_2 + y_2x_3 + y_3\left(ax_1 - bx_2 - cx_3 - dx_1^2 + u\right), \tag{21}$$

where $\mathbf{y} = \left(y_1, y_2, y_3\right)^T$.

The derivative of the Hamiltonian with respect to the scalar control is:

$$\partial_u\mathcal{H}(t,\mathbf{x},u,\mathbf{y},\mathbf{z}) = 2ru + y_3. \tag{22}$$

The first-order optimality condition reads:

$$\partial_u\mathcal{H}\left(t,\mathbf{X}_t,U_t^*,\mathbf{Y}_t,\mathbf{Z}_t\right) = 0. \tag{23}$$

Hence, the optimal feedback law is:

$$U_t^* = -\frac{1}{2r}Y_{3,t}. \tag{24}$$

This formula is the key link between the backward and forward components. Because the control acts precisely in the third channel, the third adjoint component $Y_{3,t}$ measures the marginal future value of perturbations in the active nonlinear direction. Then, substituting the feedback law into the forward equation (see Eq. (5)) yields $d\mathbf{X}_t = \mathbf{f}\left(\mathbf{X}_t, -\frac{1}{2r}Y_{3,t}\right)dt + \boldsymbol{\Sigma}dW_t$.

The gradient of the Hamiltonian with respect to the state vector is:

$$\nabla_{\mathbf{x}}\mathcal{H} = 2\mathbf{Q}\big(\mathbf{x} - \overline{\mathbf{x}}(t)\big) + \big(\nabla_{\mathbf{x}}\mathbf{f}(\mathbf{x}, u)\big)^T \mathbf{y}, \tag{25}$$

since the diffusion tensor is independent of the state variable in the present model.
The Jacobian tensor of the drift field is:

$$\nabla_{\mathbf{x}}\mathbf{f}(\mathbf{x}, u) = \begin{bmatrix} 0 & 1 & 0 \\ 0 & 0 & 1 \\ a - 2dx_1 & -b & -c \end{bmatrix}. \tag{26}$$

Therefore, we have:

$$\big(\nabla_{\mathbf{x}}\mathbf{f}(\mathbf{x}, u)\big)^T \mathbf{y} = \begin{bmatrix} (a - 2dx_1)y_3 \\ y_1 - by_3 \\ y_2 - cy_3 \end{bmatrix}. \tag{27}$$

The backward adjoint equation becomes:

$$d\mathbf{Y}_t = -\nabla_{\mathbf{x}}\mathcal{H}\big(t, \mathbf{X}_t, U_t^*, \mathbf{Y}_t, \mathbf{Z}_t\big)dt + \mathbf{Z}_t dW_t, \tag{28}$$

with terminal condition:

$$\mathbf{Y}_T = 2\mathbf{G}\big(\mathbf{X}_T - \overline{\mathbf{x}}(T)\big). \tag{29}$$

Consequently, the fully coupled FBSDE is given componentwise by:

$$\begin{aligned}
dX_{1,t} &= X_{2,t}dt, \\
dX_{2,t} &= X_{3,t}dt, \\
dX_{3,t} &= \Big(aX_{1,t} - bX_{2,t} - cX_{3,t} - dX_{1,t}^2 + U_t^*\Big)dt + \sigma dW_t, \\
dY_{1,t} &= -\big(2\big[\mathbf{Q}\big(\mathbf{X}_t - \overline{\mathbf{x}}(t)\big)_1\big] + (a - 2dX_{1,t})Y_{3,t}\big)dt + Z_{1,t}dW_t, \\
dY_{2,t} &= -\big(2\big[\mathbf{Q}\big(\mathbf{X}_t - \overline{\mathbf{x}}(t)\big)_2\big] + Y_{1,t} - bY_{3,t}\big)dt + Z_{2,t}dW_t, \\
dY_{3,t} &= -\big(2\big[\mathbf{Q}\big(\mathbf{X}_t - \overline{\mathbf{x}}(t)\big)_3\big] + Y_{2,t} - cY_{3,t}\big)dt + Z_{3,t}dW_t, \\
\mathbf{X}_0 &= \boldsymbol{\xi},\ \mathbf{Y}_T = 2\mathbf{G}\big(\mathbf{X}_T - \overline{\mathbf{x}}(T)\big).
\end{aligned} \tag{30}$$

When $\mathbf{Q}$ is diagonal with entries $q_1, q_2, q_3 \geq 0$, one has:

$$\begin{aligned}
2\big[\mathbf{Q}\big(\mathbf{X}_t - \overline{\mathbf{x}}(t)\big)_1\big] &= 2q_1\big(X_{1,t} - \overline{x}_1(t)\big), \\
2\big[\mathbf{Q}\big(\mathbf{X}_t - \overline{\mathbf{x}}(t)\big)_2\big] &= 2q_2\big(X_{2,t} - \overline{x}_2(t)\big), \\
2\big[\mathbf{Q}\big(\mathbf{X}_t - \overline{\mathbf{x}}(t)\big)_3\big] &= 2q_3\big(X_{3,t} - \overline{x}_3(t)\big).
\end{aligned} \tag{31}$$

In this common case the backward system reads:

$$\begin{aligned}
dY_{1,t} &= -\big(2q_1\big(X_{1,t} - \overline{x}_1(t)\big) + (a - 2dX_{1,t})Y_{3,t}\big)dt + Z_{1,t}dW_t, \\
dY_{2,t} &= -\big(2q_2\big(X_{2,t} - \overline{x}_2(t)\big) + Y_{1,t} - bY_{3,t}\big)dt + Z_{2,t}dW_t, \\
dY_{3,t} &= -\big(2q_3\big(X_{3,t} - \overline{x}_3(t)\big) + Y_{2,t} - cY_{3,t}\big)dt + Z_{3,t}dW_t.
\end{aligned} \tag{32}$$

Then, the terminal condition becomes:

$$\mathbf{Y}_T = 2\begin{bmatrix} g_{11} & g_{12} & g_{13} \\ g_{21} & g_{22} & g_{23} \\ g_{31} & g_{32} & g_{33} \end{bmatrix}\big(\mathbf{X}_T - \overline{\mathbf{x}}(T)\big), \tag{33}$$

where g_{ij} denotes the $(i,\ j)$-entry of the terminal tensor $\mathbf{G}$. If $\mathbf{G}$ is diagonal, then:

$$\begin{aligned}
Y_{1,T} &= 2g_1\big(X_{1,T} - \overline{x}_1(T)\big), \\
Y_{2,T} &= 2g_2\big(X_{2,T} - \overline{x}_2(T)\big), \\
Y_{3,T} &= 2g_3\big(X_{3,T} - \overline{x}_3(T)\big).
\end{aligned} \tag{34}$$

For analytical purposes, it is convenient to separate the linear and nonlinear parts of the forward drift. Define the tensor $\mathbf{A}$, the control tensor $\mathbf{B}$, and the nonlinear field $\boldsymbol{\phi}(\mathbf{x})$:

$$\mathbf{A} = \begin{bmatrix} 0 & 1 & 0 \\ 0 & 0 & 1 \\ a & -b & -c \end{bmatrix},$$

$$\mathbf{B} = \begin{bmatrix} 0 \\ 0 \\ 1 \end{bmatrix},$$
$$\boldsymbol{\phi}(\mathbf{x}) = \begin{bmatrix} 0 \\ 0 \\ -dx_1^2 \end{bmatrix}. \tag{35}$$

Then, we have:

$$\mathbf{f}(\mathbf{x}, u) = \mathbf{A}\mathbf{x} + \boldsymbol{\phi}(\mathbf{x}) + \mathbf{B}u. \tag{36}$$

The optimal control can be rewritten as $U_t^* = -\frac{1}{2r}\mathbf{B}^T\mathbf{Y}_t$, because $\mathbf{B}^T\mathbf{Y}_t = Y_{3,t}$ (see Eq. (24)). Hence the optimal forward equation becomes:

$$d\mathbf{X}_t = \left(\mathbf{A}\mathbf{X}_t + \boldsymbol{\phi}(\mathbf{X}_t) - \frac{1}{2r}\mathbf{B}\mathbf{B}^T\mathbf{Y}_t\right)dt + \boldsymbol{\Sigma}d\mathbf{W}_t. \tag{37}$$

The Jacobian of $\boldsymbol{\phi}$ is:

$$\nabla\boldsymbol{\phi}(\mathbf{x}) = \begin{bmatrix} 0 & 0 & 0 \\ 0 & 0 & 0 \\ -2dx_1 & 0 & 0 \end{bmatrix}. \tag{38}$$

Therefore, the backward equation may be expressed compactly as:

$$d\mathbf{Y}_t = -\left(2\mathbf{Q}\left(\mathbf{X}_t - \bar{\mathbf{x}}(t)\right) + \mathbf{A}^T\mathbf{Y}_t + \left(\nabla\boldsymbol{\phi}(\mathbf{X}_t)\right)^T\mathbf{Y}_t\right)dt + \mathbf{Z}_t d\mathbf{W}_t. \tag{39}$$

Since:

$$\mathbf{A}^T = \begin{bmatrix} 0 & 0 & a \\ 1 & 0 & -b \\ 0 & 1 & -c \end{bmatrix},$$
$$(\nabla\boldsymbol{\phi}(\mathbf{x}))^T = \begin{bmatrix} 0 & 0 & -2dx_1 \\ 0 & 0 & 0 \\ 0 & 0 & 0 \end{bmatrix}, \tag{40}$$

one has:

$$\mathbf{A}^T\mathbf{y} + (\nabla\boldsymbol{\phi}(\mathbf{x}))^T\mathbf{y} = \begin{bmatrix} (a - 2dx_1)y_3 \\ y_1 - by_3 \\ y_2 - cy_3 \end{bmatrix}. \tag{41}$$

Therefore, the complete compact tensor formulation is:

$$\begin{cases} d\mathbf{X}_t = \left(\mathbf{A}\mathbf{X}_t + \boldsymbol{\phi}(\mathbf{X}_t) - \frac{1}{2r}\mathbf{B}\mathbf{B}^T\mathbf{Y}_t\right)dt + \boldsymbol{\Sigma}d\mathbf{W}_t, \\ d\mathbf{Y}_t = -\left(2\mathbf{Q}\left(\mathbf{X}_t - \bar{\mathbf{x}}(t)\right) + \mathbf{A}^T\mathbf{Y}_t + \left(\nabla\boldsymbol{\phi}(\mathbf{X}_t)\right)^T\mathbf{Y}_t\right)dt + \mathbf{Z}_t d\mathbf{W}_t, \\ \mathbf{X}_0 = \boldsymbol{\xi}, \\ \mathbf{Y}_T = 2\mathbf{G}\left(\mathbf{X}_T - \bar{\mathbf{x}}(T)\right). \end{cases} \tag{42}$$

This representation makes the source of the full coupling transparent. The forward drift depends directly on the backward variable through $\mathbf{B}\mathbf{B}^T\mathbf{Y}_t$, while the backward generator depends on the forward state through both the tracking term and the nonlinear Jacobian.

4. Variational derivation and local solvability

The Hamiltonian-based derivation has been presented above. This section provides a variational derivation to clarify the adjoint structure and further support the rigor of the formulation. Let $U_t^\varepsilon = U_t + \varepsilon V_t$, where $V_t \in \mathcal{U}$ is an admissible perturbation and $\varepsilon \in \mathbb{R}$ is sufficiently small. Let $\mathbf{X}_t^\varepsilon$ denote the corresponding perturbed state. The first variation of the state is defined by:

$$\delta\mathbf{X}_t = \left.\frac{d}{d\varepsilon}\mathbf{X}_t^\varepsilon\right|_{\varepsilon=0}. \tag{43}$$

The perturbed forward dynamics satisfy:

$$d\mathbf{X}_t^\varepsilon = \mathbf{f}\left(\mathbf{X}_t^\varepsilon, U_t + \varepsilon V_t\right)dt + \boldsymbol{\Sigma}d\mathbf{W}_t. \tag{44}$$

Differentiation at $\varepsilon = 0$ yields the linearized variational equation:

$$d\left(\delta\mathbf{X}_t\right) = \left(\nabla_{\mathbf{x}}\mathbf{f}\left(\mathbf{X}_t, U_t\right)\delta\mathbf{X}_t + \mathbf{B}V_t\right)dt,$$
$$\delta\mathbf{X}_0 = \mathbf{0}. \tag{45}$$

The first variation of the objective functional is:

$$\delta J = \mathbb{E}\left[\int_0^T \left(2\left(\mathbf{X}_t - \overline{\mathbf{x}}(t)\right)^T \mathbf{Q}\delta\mathbf{X}_t + 2rU_tV_t\right)dt + 2\left(\mathbf{X}_T - \overline{\mathbf{x}}(T)\right)^T \mathbf{G}\delta\mathbf{X}_T\right]. \tag{46}$$

Now define the adjoint process $\mathbf{Y}_t$ through:

$$d\mathbf{Y}_t = -\left(2\mathbf{Q}\left(\mathbf{X}_t - \overline{\mathbf{x}}(t)\right) + \nabla_{\mathbf{x}}\mathbf{f}\left(\mathbf{X}_t, U_t\right)^T \mathbf{Y}_t\right)dt + \mathbf{Z}_t dW_t, \tag{47}$$

with terminal condition given by Eq. (29).
Applying Itô's product rule to $\mathbf{Y}_t^T\delta\mathbf{X}_t$ gives:

$$d\left(\mathbf{Y}_t^T\delta\mathbf{X}_t\right) = \mathbf{Y}_t^T d\left(\delta\mathbf{X}_t\right) + \delta\mathbf{X}_t^T d\mathbf{Y}_t + d\langle\mathbf{Y}, \delta\mathbf{X}\rangle_t. \tag{48}$$

Since $\delta\mathbf{X}_t$ has no diffusion term in the present additive-noise configuration, the quadratic covariation vanishes, $d\langle\mathbf{Y}, \delta\mathbf{X}\rangle_t = 0$. Substituting the forward and backward equations yields:

$$\begin{aligned} &d\left(\mathbf{Y}_t^T\delta\mathbf{X}_t\right) \\ &= \left(\mathbf{Y}_t^T\nabla_{\mathbf{x}}\mathbf{f}\left(\mathbf{X}_t, U_t\right)\delta\mathbf{X}_t + \mathbf{Y}_t^T\mathbf{B}V_t - \delta\mathbf{X}_t^T\left[2\mathbf{Q}\left(\mathbf{X}_t - \overline{\mathbf{x}}(t)\right) + \nabla_{\mathbf{x}}\mathbf{f}\left(\mathbf{X}_t, U_t\right)^T\mathbf{Y}_t\right]\right)dt \\ &\quad + \delta\mathbf{X}_t^T\mathbf{Z}_t dW_t. \end{aligned} \tag{49}$$

The Jacobian terms cancel, and one obtains:

$$d\left(\mathbf{Y}_t^T\delta\mathbf{X}_t\right) = \left(\mathbf{Y}_t^T\mathbf{B}V_t - 2\left(\mathbf{X}_t - \overline{\mathbf{x}}(t)\right)^T\mathbf{Q}\delta\mathbf{X}_t\right)dt + \delta\mathbf{X}_t^T\mathbf{Z}_t dW_t. \tag{50}$$

After integration over $[0, T]$, expectation, and use of $\delta\mathbf{X}_0 = \mathbf{0}$, we obtain:

$$\mathbb{E}\left[\mathbf{Y}_T^T\delta\mathbf{X}_T\right] = \mathbb{E}\left[\int_0^T \left(\mathbf{Y}_t^T\mathbf{B}V_t - 2\left(\mathbf{X}_t - \overline{\mathbf{x}}(t)\right)^T\mathbf{Q}\delta\mathbf{X}_t\right)dt\right]. \tag{51}$$

The terminal condition implies:

$$\mathbb{E}\left[2\left(\mathbf{X}_T - \overline{\mathbf{x}}(T)\right)^T\mathbf{G}\delta\mathbf{X}_T\right] = \mathbb{E}\left[\int_0^T \left(\mathbf{Y}_t^T\mathbf{B}V_t - 2\left(\mathbf{X}_t - \overline{\mathbf{x}}(t)\right)^T\mathbf{Q}\delta\mathbf{X}_t\right)dt\right]. \tag{52}$$

Substituting Eq. (52) into δJ (see Eq. (46)) gives:

$$\delta J = \mathbb{E}\left[\int_0^T \left(2rU_t + \mathbf{B}^T\mathbf{Y}_t\right)V_t dt\right]. \tag{53}$$

Because V_t is arbitrary, the first-order condition is $2rU_t^* + \mathbf{B}^T\mathbf{Y}_t = 0$, and therefore $U_t^* = -\frac{1}{2r}\mathbf{B}^T\mathbf{Y}_t$.
Next, we discuss the structural conditions needed for local well-posedness. Define:

$$\begin{aligned} \mathbf{b}(t, \mathbf{x}, \mathbf{y}) &= \mathbf{A}\mathbf{x} + \boldsymbol{\phi}(\mathbf{x}) - \frac{1}{2r}\mathbf{B}\mathbf{B}^T\mathbf{y}, \\ \mathbf{g}(t, \mathbf{x}, \mathbf{y}) &= 2\mathbf{Q}\left(\mathbf{x} - \overline{\mathbf{x}}(t)\right) + \mathbf{A}^T\mathbf{y} + \left(\nabla\boldsymbol{\phi}(\mathbf{x})\right)^T\mathbf{y}, \\ \mathbf{h}(\mathbf{x}) &= 2\mathbf{G}\left(\mathbf{x} - \overline{\mathbf{x}}(T)\right). \end{aligned} \tag{54}$$

Then, the FBSDE takes the standard form:

$$\begin{aligned} d\mathbf{X}_t &= \mathbf{b}\left(t, \mathbf{X}_t, \mathbf{Y}_t\right)dt + \boldsymbol{\Sigma}dW_t, \\ d\mathbf{Y}_t &= -\mathbf{g}\left(t, \mathbf{X}_t, \mathbf{Y}_t\right)dt + \mathbf{Z}_t dW_t, \\ \mathbf{X}_0 &= \boldsymbol{\xi},\ \mathbf{Y}_T = \mathbf{h}\left(\mathbf{X}_T\right). \end{aligned} \tag{55}$$

Assume that the solution remains in the bounded cylinder:

$$D_R = \left\{(t, \mathbf{x}, \mathbf{y}) \in [0, T] \times \mathbb{R}^3 \times \mathbb{R}^3 : \|\mathbf{x}\| \le R,\ \|\mathbf{y}\| \le R\right\}, \tag{56}$$

for some $R > 0$. On this domain, the nonlinear field $\boldsymbol{\phi}$ is locally Lipschitz:

$$\left\|\boldsymbol{\phi}(\mathbf{x}) - \boldsymbol{\phi}(\widetilde{\mathbf{x}})\right\| \le 2|d|R\|\mathbf{x} - \widetilde{\mathbf{x}}\|. \tag{57}$$

Then, we have:

$$\left|-dx_1^2 + d\widetilde{x}_1^2\right| = |d|\left|x_1 - \widetilde{x}_1\right|\left|x_1 + \widetilde{x}_1\right| \le 2|d|R\left|x_1 - \widetilde{x}_1\right| \le 2|d|R\|\mathbf{x} - \widetilde{\mathbf{x}}\|. \tag{58}$$

Likewise, the Jacobian satisfies:

$$\left\|\nabla\boldsymbol{\phi}(\mathbf{x}) - \nabla\boldsymbol{\phi}(\widetilde{\mathbf{x}})\right\| \le 2|d|\|\mathbf{x} - \widetilde{\mathbf{x}}\|. \tag{59}$$

Therefore, the following holds:

$$\left\|\mathbf{b}(t, \mathbf{x}, \mathbf{y}) - \mathbf{b}(t, \widetilde{\mathbf{x}}, \widetilde{\mathbf{y}})\right\| \le (\|\mathbf{A}\| + 2|d|R)\|\mathbf{x} - \widetilde{\mathbf{x}}\| + \frac{1}{2r}\left\|\mathbf{B}\mathbf{B}^T\right\|\|\mathbf{y} - \widetilde{\mathbf{y}}\|. \tag{60}$$

For the backward generator, one has:

$$\mathbf{g}(t,\mathbf{x},\mathbf{y})-\mathbf{g}\left(t,\widetilde{\mathbf{x}},\widetilde{\mathbf{y}}\right)=2\mathbf{Q}\left(\mathbf{x}-\widetilde{\mathbf{x}}\right)+\mathbf{A}^{T}\left(\mathbf{y}-\widetilde{\mathbf{y}}\right)+(\nabla\boldsymbol{\phi}(\mathbf{x}))^{T}\mathbf{y}-\left(\nabla\boldsymbol{\phi}\left(\widetilde{\mathbf{x}}\right)\right)^{T}\widetilde{\mathbf{y}}. \tag{61}$$

Hence, we have:

$$\begin{aligned}&\left\|\mathbf{g}(t,\mathbf{x},\mathbf{y})-\mathbf{g}\left(t,\widetilde{\mathbf{x}},\widetilde{\mathbf{y}}\right)\right\|\\&\quad\le 2\|\mathbf{Q}\|\left\|\mathbf{x}-\widetilde{\mathbf{x}}\right\|+\|\mathbf{A}\|\left\|\mathbf{y}-\widetilde{\mathbf{y}}\right\|+\left\|\nabla\boldsymbol{\phi}(\mathbf{x})-\nabla\boldsymbol{\phi}\left(\widetilde{\mathbf{x}}\right)\right\|\|\mathbf{y}\|+\left\|\nabla\boldsymbol{\phi}\left(\widetilde{\mathbf{x}}\right)\right\|\left\|\mathbf{y}-\widetilde{\mathbf{y}}\right\|.\end{aligned} \tag{62}$$

Using the local bounds above, we have:

$$\left\|\mathbf{g}(t,\mathbf{x},\mathbf{y})-\mathbf{g}\left(t,\widetilde{\mathbf{x}},\widetilde{\mathbf{y}}\right)\right\|\le(2\|\mathbf{Q}\|+2|d|R)\left\|\mathbf{x}-\widetilde{\mathbf{x}}\right\|+(\|\mathbf{A}\|+2|d|R)\left\|\mathbf{y}-\widetilde{\mathbf{y}}\right\|. \tag{63}$$

The terminal map is Lipschitz:

$$\left\|\mathbf{h}(\mathbf{x})-\mathbf{h}\left(\widetilde{\mathbf{x}}\right)\right\|\le 2\|\mathbf{G}\|\left\|\mathbf{x}-\widetilde{\mathbf{x}}\right\|. \tag{64}$$

Define:

$$\begin{aligned}&L_b=\|\mathbf{A}\|+2|d|R+\frac{1}{2r}\left\|\mathbf{B}\mathbf{B}^{T}\right\|,\\&L_g=2\|\mathbf{Q}\|+\|\mathbf{A}\|+4|d|R,\\&L_h=2\|\mathbf{G}\|.\end{aligned} \tag{65}$$

Then, on a sufficiently short horizon, a Picard contraction argument yields local solvability. In particular, there exists $T^{*}>0$, depending on L_b, L_g, L_h, and σ, such that for every $T\in(0,T^{*}]$, the fully coupled system admits a unique square-integrable adapted solution. A schematic sufficient condition may be written as:

$$C\left(L_b+L_g+L_h\right)T^{*}<1, \tag{66}$$

where $C>0$ is a generic constant arising in the contraction estimate.
If the solution norm is measured by:

$$\|(\mathbf{X},\mathbf{Y},\mathbf{Z})\|_{\mathbb{H}}^{2}=\mathbb{E}\left[\sup_{0\le t\le T}\left\|\mathbf{X}_t\right\|^{2}+\sup_{0\le t\le T}\left\|\mathbf{Y}_t\right\|^{2}+\int_{0}^{T}\left\|\mathbf{Z}_t\right\|^{2}dt\right], \tag{67}$$

then, the Picard map Γ satisfies:

$$\left\|\Gamma(\mathbf{X},\mathbf{Y},\mathbf{Z})-\Gamma\left(\widetilde{\mathbf{X}},\widetilde{\mathbf{Y}},\widetilde{\mathbf{Z}}\right)\right\|_{\mathbb{H}}\le\kappa(T)\left\|(\mathbf{X},\mathbf{Y},\mathbf{Z})-\left(\widetilde{\mathbf{X}},\widetilde{\mathbf{Y}},\widetilde{\mathbf{Z}}\right)\right\|_{\mathbb{H}}, \tag{68}$$

with:

$$\kappa(T)=C_1T^{\frac{1}{2}}L_b+C_2T^{\frac{1}{2}}L_g+C_3T^{\frac{1}{2}}L_h. \tag{69}$$

Whenever $\kappa(T)<1$, the map Γ is a contraction. This result is especially relevant for the present ACT setting, because the nonlinearity is strong enough to preserve the spiral-chaotic character, yet sufficiently structured to permit local FBSDE analysis on bounded domains.

5. Decoupling-field interpretation and time-discrete approximation

A second important viewpoint is the decoupling-field representation. Suppose there exists a deterministic mapping $\mathbf{u}:[0,T]\times\mathbb{R}^{3}\to\mathbb{R}^{3}$ such that $\mathbf{Y}_t=\mathbf{u}\left(t,\mathbf{X}_t\right)$. If $\mathbf{u}$ is sufficiently smooth, Itô's formula gives:

$$\begin{aligned}d\mathbf{Y}_t=&\Big(\partial_t\mathbf{u}\left(t,\mathbf{X}_t\right)+\nabla_{\mathbf{x}}\mathbf{u}\left(t,\mathbf{X}_t\right)\mathbf{b}\left(t,\mathbf{X}_t,\mathbf{u}\left(t,\mathbf{X}_t\right)\right)+\frac{1}{2}Tr\left[\boldsymbol{\Sigma}\boldsymbol{\Sigma}^{T}\nabla_{\mathbf{x}}^{2}\mathbf{u}\left(t,\mathbf{X}_t\right)\right]\Big)dt\\&+\nabla_{\mathbf{x}}\mathbf{u}\left(t,\mathbf{X}_t\right)\boldsymbol{\Sigma}d\mathbf{W}_t.\end{aligned} \tag{70}$$

A comparison with the backward equation yields:

$$\mathbf{Z}_t=\nabla_{\mathbf{x}}\mathbf{u}\left(t,\mathbf{X}_t\right)\boldsymbol{\Sigma}. \tag{71}$$

The decoupling field must therefore satisfy the quasilinear PDE:

$$\partial_t\mathbf{u}+\nabla_{\mathbf{x}}\mathbf{u}\mathbf{b}(t,\mathbf{x},\mathbf{u})+\frac{1}{2}Tr\left[\boldsymbol{\Sigma}\boldsymbol{\Sigma}^{T}\nabla_{\mathbf{x}}^{2}\mathbf{u}\right]+\mathbf{g}(t,\mathbf{x},\mathbf{u})=\mathbf{0}, \tag{72}$$

with terminal condition:

$$\mathbf{u}(T,\mathbf{x})=2\mathbf{G}\left(\mathbf{x}-\overline{\mathbf{x}}(T)\right). \tag{73}$$

Substituting the explicit forms of $\mathbf{b}$ and $\mathbf{g}$, we obtain:

$$\partial_t\mathbf{u}+\nabla_{\mathbf{x}}\mathbf{u}\left(\mathbf{A}\mathbf{x}+\boldsymbol{\phi}(\mathbf{x})-\frac{1}{2r}\mathbf{B}\mathbf{B}^{T}\mathbf{u}\right)+\frac{1}{2}Tr\left[\boldsymbol{\Sigma}\boldsymbol{\Sigma}^{T}\nabla_{\mathbf{x}}^{2}\mathbf{u}\right]+2\mathbf{Q}\left(\mathbf{x}-\overline{\mathbf{x}}(t)\right)+\mathbf{A}^{T}\mathbf{u}$$

$$+ (\nabla \boldsymbol{\phi}(\mathbf{x}))^T \mathbf{u} = \mathbf{0}. \tag{74}$$

The feedback control becomes:

$$U_t^* = -\frac{1}{2r}\mathbf{B}^T \mathbf{u}(t, \mathbf{X}_t). \tag{75}$$

The decoupling-field representation shows that the backward process can be regarded as a nonlinear feedback surface defined over state space and time. From a physical standpoint, this means that the adjoint field acts as a time-dependent geometric potential encoding how future tracking cost propagates backward along the random ACT flow.

For numerical approximation, let $N \in \mathbb{N}$ be the number of time steps and define the grid:

$$t_n = n\Delta t,\ \Delta t = \frac{T}{N},\ n = 0, 1, \dots, N. \tag{76}$$

Let $\Delta W_n = W_{t_{n+1}} - W_{t_n}$. Then, we have:

$$\Delta W_n \sim \mathcal{N}(0, \Delta t),\ \mathbb{E}\left[\Delta W_n\right] = 0,\ \mathbb{E}\left[\left(\Delta W_n\right)^2\right] = \Delta t. \tag{77}$$

A Picard iteration indexed by k can be constructed as follows. The forward Euler-Maruyama step is [50]:

$$\mathbf{X}_{n+1}^{(k+1)} = \mathbf{X}_n^{(k+1)} + \left(\mathbf{A}\mathbf{X}_n^{(k+1)} + \boldsymbol{\phi}\left(\mathbf{X}_n^{(k+1)}\right) - \frac{1}{2r}\mathbf{B}\mathbf{B}^T \mathbf{Y}_n^{(k)}\right)\Delta t + \boldsymbol{\Sigma}\Delta W_n. \tag{78}$$

The terminal backward value is:

$$\mathbf{Y}_N^{(k+1)} = 2\mathbf{G}\left(\mathbf{X}_N^{(k+1)} - \overline{\mathbf{x}}(T)\right). \tag{79}$$

A discrete backward recursion can be written as:

$$\mathbf{Y}_n^{(k+1)} = \mathbb{E}_n\left[\mathbf{Y}_{n+1}^{(k+1)} + \mathbf{g}\left(t_n, \mathbf{X}_n^{(k+1)}, \mathbf{Y}_n^{(k+1)}\right)\Delta t\right], \tag{80}$$

where $\mathbb{E}_n[\cdot]$ denotes conditional expectation given $\mathcal{F}_{t_n}$.

Similarly, we have:

$$\mathbf{Z}_n^{(k+1)} = \frac{1}{\Delta t}\mathbb{E}_n\left[\mathbf{Y}_{n+1}^{(k+1)}\Delta W_n\right]. \tag{81}$$

Because these conditional expectations are not available explicitly in nonlinear ACT dynamics, a regression approximation is natural. Let $\boldsymbol{\Psi}(\mathbf{x}) \in \mathbb{R}^P$ denote a vector of P basis functions. Then one may write:

$$\begin{aligned} Y_{i,n}^{(k+1)} &\approx \left(\boldsymbol{\beta}_{i,n}^{(k+1)}\right)^T \boldsymbol{\Psi}\left(\mathbf{X}_n^{(k+1)}\right)\ for\ i = 1, 2, 3, \\ Z_{i,n}^{(k+1)} &\approx \left(\boldsymbol{\gamma}_{i,n}^{(k+1)}\right)^T \boldsymbol{\Psi}\left(\mathbf{X}_n^{(k+1)}\right)\ for\ i = 1, 2, 3, \end{aligned} \tag{82}$$

where $\boldsymbol{\beta}_{i,n}^{(k+1)}$ and $\boldsymbol{\gamma}_{i,n}^{(k+1)}$ are coefficient vectors.

In the numerical experiments of this paper, the regression basis is chosen as a low-order polynomial family built from both the current forward state and the instantaneous tracking error. More precisely, let $\mathbf{X}_n = \left(x_1, x_2, x_3\right)^T$ denote the forward state at time level t_n, and let $\mathbf{E}_n = \left(e_1, e_2, e_3\right)^T = \mathbf{X}_n - \overline{\mathbf{x}}\left(t_n\right)$ denote the deviation from the reference orbit. Before regression, each scalar component is standardized by subtracting its sample mean and dividing by its sample standard deviation, in order to reduce scale imbalance and improve numerical conditioning. Denoting the standardized variables by $x_{1,s}$, $x_{2,s}$, $x_{3,s}$, $e_{1,s}$, $e_{2,s}$, $e_{3,s}$, the basis vector used in all computations is taken as:

$$\boldsymbol{\Psi} = \left[1, x_{1,s}, x_{2,s}, x_{3,s}, e_{1,s}, e_{2,s}, e_{3,s}, x_{1,s}^2, x_{2,s}^2, x_{3,s}^2, x_{1,s}x_{2,s}, x_{1,s}x_{3,s}, x_{2,s}x_{3,s}\right]^T. \tag{83}$$

Thus, the regression space contains one constant term, three linear state terms, three linear tracking-error terms, three quadratic state terms, and three pairwise bilinear interaction terms, giving a total of $P = 13$ basis functions. This choice was adopted throughout the numerical study because it is rich enough to capture the main local nonlinearity of the ACT dynamics and the state-reference mismatch, while remaining sufficiently low-dimensional for stable ridge-regularized least-squares fitting in each backward step.

For a Monte Carlo ensemble $\left\{\mathbf{X}_n^m\right\}_{m=1}^M$, the regression coefficients minimize $\sum_{m=1}^M \left|\boldsymbol{\beta}_{i,n}^T \boldsymbol{\Psi}\left(\mathbf{X}_n^m\right) - \mathcal{T}_{i,n}^m\right|^2$, where $\mathcal{T}_{i,n}^m$ is the backward target. With an explicit generator approximation, one has:

$$\mathcal{T}_n^m = \mathbf{Y}_{n+1}^m + \mathbf{g}\left(t_n, \mathbf{X}_n^m, \mathbf{Y}_{n+1}^m\right)\Delta t. \tag{84}$$

For the martingale coefficient, one uses:

$$\mathcal{S}_n^m = \frac{1}{\Delta t}\mathbf{Y}_{n+1}^m \Delta W_n^m. \tag{85}$$

Let:

$$\boldsymbol{\Psi}_n = \begin{bmatrix} \boldsymbol{\Psi}\left(\mathbf{X}_n^1\right)^T \\ \boldsymbol{\Psi}\left(\mathbf{X}_n^2\right)^T \\ \vdots \\ \boldsymbol{\Psi}\left(\mathbf{X}_n^M\right)^T \end{bmatrix} \in \mathbb{R}^{M \times P}. \tag{86}$$

Then, the normal equations take the form:

$$\boldsymbol{\beta}_{i,n} = \left(\boldsymbol{\Psi}_n^T \boldsymbol{\Psi}_n\right)^{-1} \boldsymbol{\Psi}_n^T \mathbf{T}_{i,n},$$
$$\boldsymbol{\gamma}_{i,n} = \left(\boldsymbol{\Psi}_n^T \boldsymbol{\Psi}_n\right)^{-1} \boldsymbol{\Psi}_n^T \mathbf{S}_{i,n}, \tag{87}$$

where $\mathbf{T}_{i,n} \in \mathbb{R}^M$ and $\mathbf{S}_{i,n} \in \mathbb{R}^M$ are the sampled target vectors.

After the backward coefficients are computed, the discrete feedback update is $U_n^{(k+1)} = -\frac{1}{2r}\mathbf{B}^T \mathbf{Y}_n^{(k+1)}$. A practical stopping rule is:

$$\frac{\sum_{n=0}^{N-1} \left|U_n^{(k+1)} - U_n^{(k)}\right|^2}{\sum_{n=0}^{N-1} \left|U_n^{(k)}\right|^2 + \varepsilon_0} < Tol, \tag{88}$$

where $\varepsilon_0 > 0$ is a small regularization constant and $Tol > 0$ is a prescribed tolerance.

Under standard bounded-domain assumptions, the forward strong approximation satisfies:

$$\max_{0 \le n \le N} \mathbb{E}\left\|\mathbf{X}_{t_n} - \mathbf{X}_n\right\|^2 = O(\Delta t). \tag{89}$$

The total error can be represented schematically as:

$$\mathcal{E}_{tot} \le C_1 (\Delta t)^{\frac{1}{2}} + C_2 \mathcal{E}_{reg} + C_3 \mathcal{E}_{Pic}, \tag{90}$$

where $\mathcal{E}_{reg}$ is the regression error and $\mathcal{E}_{Pic}$ is the Picard residual.

6. Numerical experiments

Based on the parameter settings reported in Table 2, a series of numerical experiments was conducted to assess the dynamical behavior of the proposed model and to verify the effectiveness of the analytical framework developed in this study. The numerical results were organized to examine the deterministic and stochastic ACT attractor structures, the baseline performance of the coupled FBSDE control strategy, and the sensitivity of the controlled system to key model and weighting parameters. Particular attention was given to orbit morphology, random-attractor characteristics, tracking performance, adjoint-state behavior, control-energy distribution, and the response-surface patterns associated with parameter variation. Taken together, these experiments provide a unified illustration of how the theoretical formulation is reflected in the geometry, stability, and control properties of the ACT system under stochastic perturbations.

It should be emphasized that the fully coupled solver is implemented here as a damped finite-horizon Picard procedure rather than as a global convergence method for arbitrary chaotic regimes. Although classical FBSDE theory only guarantees Picard convergence under restrictive conditions, the present computations remain stable in practice because several numerical safeguards are used simultaneously. In particular, the time step is kept sufficiently small, the number of Picard iterations is moderate, the backward update is relaxed through the damping factor θ_{Picard}, and the forward state, backward state, and control are clipped by the thresholds x_{cap}, y_{cap}, and u_{cap}, respectively. In addition, the regression step is stabilized by ridge regularization with parameter λ_{ridge}, and the basis variables are standardized before the least-squares fit, which reduces ill-conditioning during the backward recursion. Therefore, the numerical results reported below should be interpreted as computations obtained in a stabilized finite-horizon regime for which the Picard iteration remains empirically controlled under the selected parameter set, rather than as evidence of unconditional convergence for long-horizon chaotic FBSDEs.

6.1. Deterministic and stochastic ACT attractor structure

Fig. 1 illustrates the geometric evolution of the deterministic ACT attractor when the parameter a is varied, while the remaining model parameters are kept fixed. Here, a denotes the linear excitation coefficient in the third state equation, and it directly affects the overall stretching intensity of the flow. From the six subplots, it is clear that the deterministic ACT system preserves a spiral-type attractor structure over the selected parameter interval, but the detailed orbit morphology changes noticeably as a increases. This indicates that the attractor is not rigid with respect to parameter perturbation, and that even moderate changes in linear excitation can alter the balance between local rotation and global reinjection.

A first important feature is that the attractor remains bounded throughout the displayed range of a, which suggests that the chosen parameter window corresponds to a dynamically persistent nonlinear regime rather than a transient escape or divergence regime. At the lower values of a, the phase trajectories exhibit a relatively compact spiral organization, with repeated winding around a central region and a comparatively regular large-scale return. As a is increased, the attractor becomes more stretched, and the orbit branches extend further along the longitudinal direction of the phase space. This reflects a strengthening of the global excursion mechanism, meaning that trajectories are driven farther away before being reinjected into the central rotating region.

Another notable observation is that the attractor morphology is not monotonic in a purely geometric sense. The panels corresponding to intermediate values of a show partial deformation and temporary simplification of the orbit structure, whereas larger values recover a more developed spiral-chaotic shape with broader excursion layers. In particular, the case around $a = 5.60$ appears comparatively less complex than the neighboring cases, which suggests that the deterministic ACT flow may pass through a transitional regime in which the orbit organization becomes temporarily less folded. This type of behavior is consistent with the fact that parameter variation in nonlinear chaotic oscillators often produces alternating windows of stronger and weaker geometric complexity.

Table 2
Parameter settings.

Symbol	Meaning	Value
a	Linear excitation parameter in the ACT drift	5.65
b	Linear coupling-damping parameter in the ACT drift	3.35
c	Direct damping parameter in the third channel	0.95
d	Nonlinear coefficient in the third equation	1.00
σ	Diffusion intensity	0.10
$\mathbf{Q}$	Running-state tracking weight tensor	$diag(2.20, 0.55, 0.45)$
$\mathbf{G}$	Terminal-state tracking weight tensor	$diag(4.20, 1.25, 1.10)$
r	Control penalty coefficient	0.90
T	Time horizon for the baseline FBSDE simulation	20
N	Number of time steps in the baseline FBSDE simulation	400
$\mathbf{x}_0$	Initial state for the controlled forward process	$[0.23, 0.00, 0.00]^T$
$\bar{\mathbf{x}}(0)$	Initial seed used to construct the reference orbit	$[0.18, 0.03, 0.00]^T$
M	Monte Carlo sample size for the baseline solve	10,000
$K_{\max}$	Maximum Picard iterations for the baseline solve	6
λ_{ridge}	Ridge regularization used in regression	10^{-6}
θ_{Picard}	Picard damping factor	0.70
u_{cap}	Numerical clipping threshold for the control	11.0
y_{cap}	Numerical clipping threshold for the backward state	18.0
x_{cap}	Numerical clipping threshold for the forward state	12.0
ϵ_0	Initial perturbation amplitude	10^{-5}

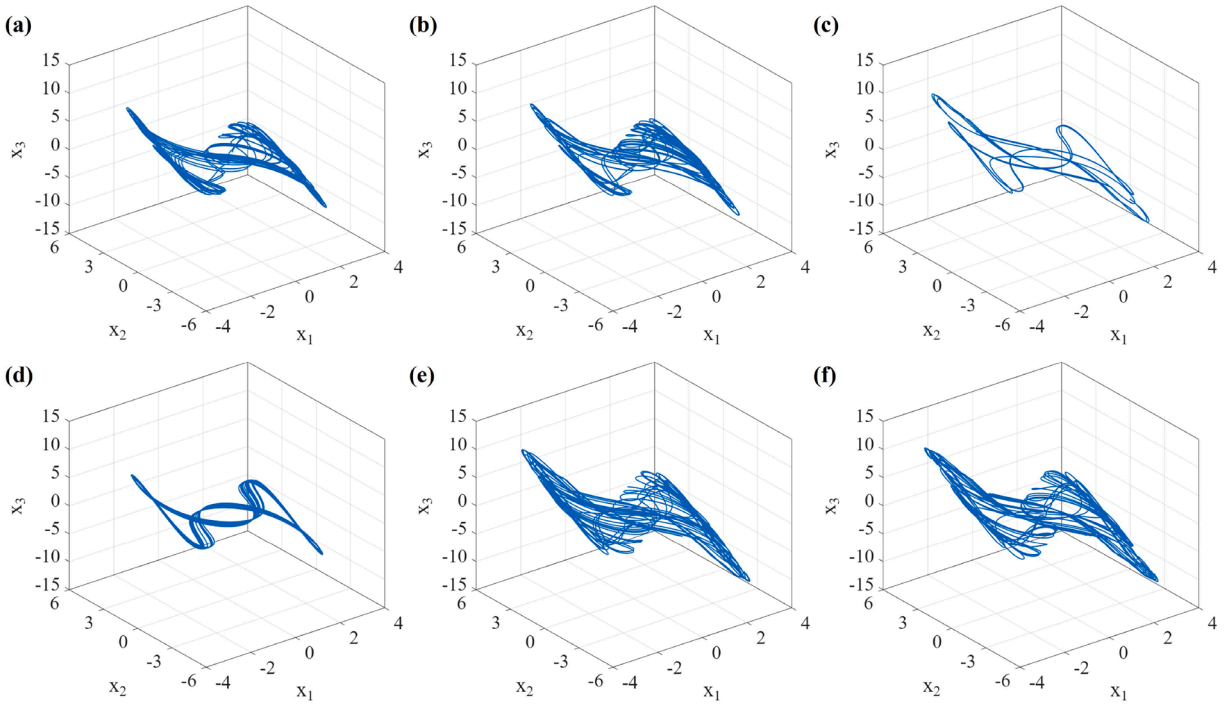

Fig. 1. Deterministic ACT attractor morphology under variation of a: (a) $a = 5.00$; (b) $a = 5.20$; (c) $a = 5.40$; (d) $a = 5.60$; (e) $a = 5.80$; (f) $a = 6.00$.

From the viewpoint of the present study, Fig. 1 serves two purposes. First, it confirms that the ACT model provides a suitable deterministic skeleton for constructing a reference orbit with nontrivial spiral geometry. Second, it shows that the parameter a has a visible and dynamically meaningful influence on attractor morphology, which justifies its later use in sensitivity and response-surface analysis. Overall, the figure demonstrates that the deterministic ACT system possesses a stable but shape-sensitive spiral attractor family, providing an appropriate foundation for the subsequent stochastic and FBSDE-based orbit-steering analysis.

Fig. 2 provides a more detailed diagnostic view of the deterministic ACT attractor at the baseline parameter set. While Fig. 1 primarily illustrated how the global attractor morphology changes under variation of a, the present figure focuses on the internal geometric and temporal structure of a single representative regime. Taken together, the six panels show that the baseline ACT dynamics possess a well-developed spiral-chaotic organization, combining bounded long-time motion, repeated oscillatory excursions, and nontrivial return behavior in phase space.

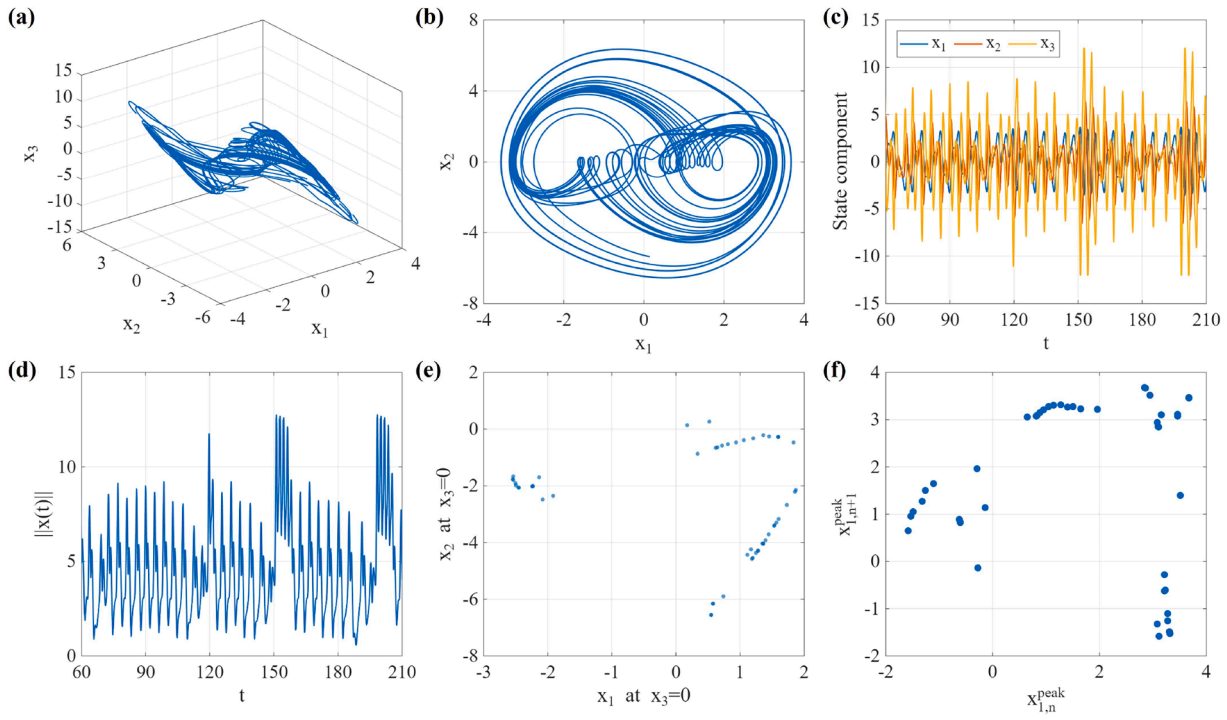

Fig. 2. Baseline deterministic diagnostics of the ACT attractor: (a) 3D ACT attractor at baseline parameters; (b) projection on the $x_1 - x_2$ plane; (c) temporal evolution of deterministic ACT states; (d) state radius along the attractor; (e) Poincaré section from upward x_3 crossings; (f) return map of successive local maxima.

The three-dimensional portrait in the first panel confirms that the attractor is organized around a spiral-reinjection mechanism rather than around a simple closed orbit. The trajectory repeatedly stretches away from the central region and then returns through folded branches, indicating a persistent interaction between local rotation and global transport. This interpretation is reinforced by the projection onto the x_1-x_2 plane shown in the second panel, where the orbit occupies a broad two-lobed region with visible overlap and repeated winding. Such a projection highlights the fact that the attractor is not confined to a narrow annular structure, but instead explores a comparatively wide part of the reduced phase plane.

The temporal evolution of the three state components in the third panel shows sustained irregular oscillations over the displayed interval. The components x_1, x_2, and x_3 remain bounded, but their amplitudes and local oscillation frequencies vary over time, which is consistent with deterministic chaotic behavior rather than quasiperiodic motion. In particular, the third component x_3 exhibits the largest excursions, reaching visibly higher positive and negative amplitudes than the other two components. This is dynamically meaningful because the nonlinear ACT drift is driven through the third equation, so the stronger variation in x_3 reflects the active role of that channel in shaping the attractor geometry.

The fourth panel, which shows the state radius $\|\mathbf{x}(t)\|$, provides a compact measure of how far the trajectory moves from the origin over time. The radius oscillates in an irregular but bounded manner, with repeated bursts corresponding to large excursions of the orbit away from the central spiral region. The presence of alternating moderate and large peaks suggests that the deterministic flow repeatedly switches between relatively compact rotation and more extended reinjection episodes. This observation supports the visual evidence from the first panel and confirms that the attractor dynamics are strongly nonuniform along the orbit.

The last two panels further clarify the return structure of the deterministic ACT flow. The Poincaré section, constructed from upward crossings of the plane $x_3 = 0$, produces a scattered but organized point set rather than a single isolated point or a smooth closed curve. This indicates that the return dynamics on the chosen section are nontrivial and possess a clear low-dimensional geometric pattern. The return map of successive local maxima of x_1, denoted by $x_{1,n}^{peak}$ and $x_{1,n+1}^{peak}$, shows a dispersed point cloud with evident nonlinear structure. Here, $x_{1,n}^{peak}$ represents the nth local maximum of x_1. The absence of collapse onto a single branch is consistent with irregular deterministic recurrence and further supports the interpretation that the baseline regime is suitable for representing a genuinely chaotic ACT attractor. Overall, Fig. 2 establishes the baseline deterministic regime as dynamically rich, geometrically structured, and appropriate for constructing the reference orbit used in the subsequent stochastic control analysis.

Fig. 3 shows how the ACT attractor geometry changes when stochastic perturbation is introduced and the diffusion intensity σ is gradually increased. Here, σ denotes the noise intensity in the third state equation, and therefore it directly controls the strength of random forcing acting on the most dynamically active channel of the system. The six panels indicate that the global attractor remains bounded over the entire range considered, but its internal orbit structure becomes progressively more diffuse as the stochastic

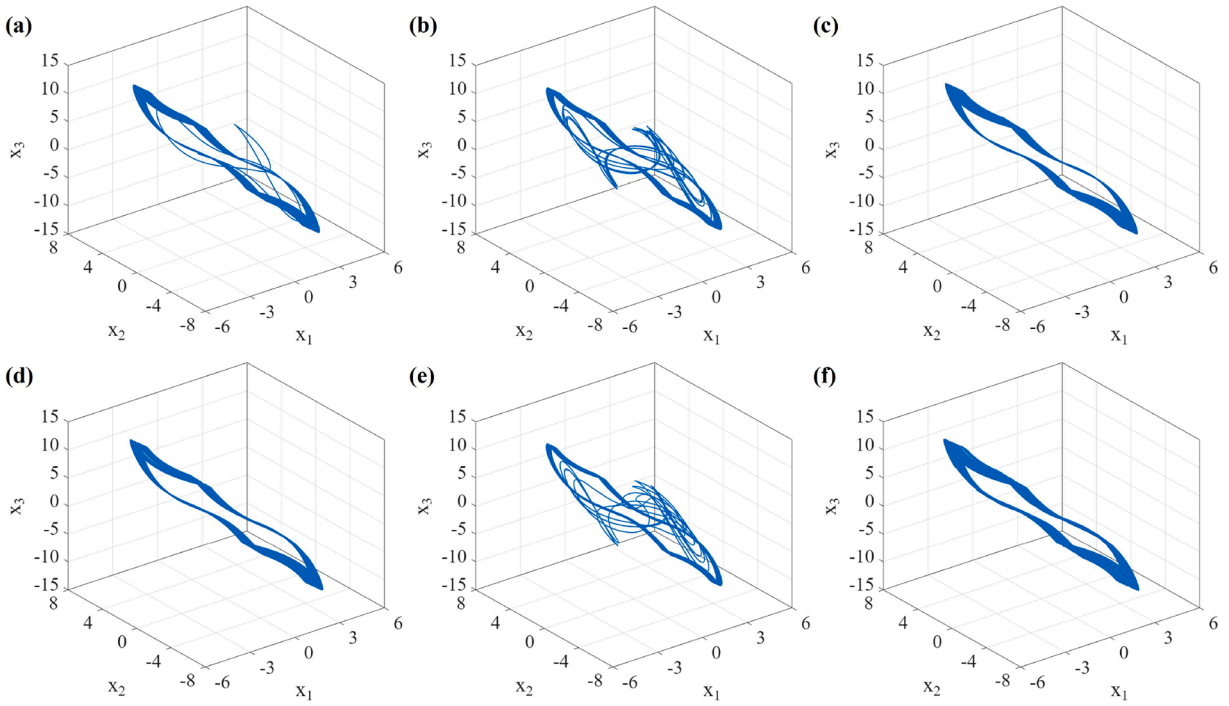

Fig. 3. Stochastic ACT attractor morphology under increasing noise intensity: (a) $\sigma = 0.000$; (b) $\sigma = 0.025$; (c) $\sigma = 0.050$; (d) $\sigma = 0.075$; (e) $\sigma = 0.100$; (f) $\sigma = 0.140$.

contribution becomes stronger. This confirms that the ACT flow is robust enough to preserve its large-scale phase-space organization under moderate noise, while still exhibiting visible deformation at the level of local trajectory geometry.

A first important observation is that the stochastic attractor retains the same broad spiral-reinjection skeleton as in the deterministic regime. Even for the larger values of σ, the trajectories continue to evolve within a structured elongated region rather than dispersing into an unorganized cloud. This suggests that the deterministic ACT attractor acts as a persistent geometric backbone for the noisy dynamics. In other words, noise does not destroy the overall phase-space architecture immediately, but instead broadens the neighborhood in which the trajectories move. This feature is especially relevant for the present study, because the proposed stochastic control framework is built on the idea of steering trajectories near a reference orbit extracted from the deterministic attractor.

At the same time, the figure also shows that the effect of noise is not purely monotonic in visual appearance. For smaller values such as $\sigma = 0.025$, the trajectories already exhibit noticeable transverse spreading and local irregularity relative to the deterministic case. Around intermediate noise levels, the stochastic orbit may appear either more diffuse or temporarily more compressed depending on how the random perturbation interacts with the reinjection mechanism over the finite observation window. This is a typical feature of stochastic chaotic trajectories, since finite-time realizations do not always display a simple unidirectional broadening with respect to the noise parameter. Nevertheless, the overall tendency remains clear: increasing σ leads to a thicker and less sharply organized attractor neighborhood.

Another relevant point is that the random perturbation acts in the third channel, but its geometric influence extends to the full three-dimensional orbit. This indicates that the system redistributes stochastic perturbations through the nonlinear coupling of the ACT dynamics. As a result, noise injected into x_3 is transmitted to the entire phase trajectory, altering both the local winding structure and the reinjection pattern. From the viewpoint of control design, this observation is important because it shows that regulation of the third channel is sufficient to influence the full orbit geometry, which is fully consistent with the later optimal feedback law derived from the coupled FBSDE formulation.

Overall, Fig. 3 demonstrates that the stochastic ACT system preserves a recognizable attractor morphology under increasing diffusion intensity, but that the attractor becomes progressively less sharply defined as random forcing increases. This balance between persistence and deformation is precisely the setting in which stochastic orbit steering becomes meaningful. The figure therefore provides the necessary dynamical motivation for studying how the coupled FBSDE framework can control trajectory dispersion while still respecting the intrinsic spiral structure of the ACT attractor.

Fig. 4 gives a more detailed characterization of the stochastic ACT dynamics at the baseline noise level from the perspective of a random attractor. In contrast to the previous figure, which emphasized the visual effect of increasing diffusion intensity, the present figure focuses on the internal geometric, temporal, and statistical structure of the noisy attractor under a fixed stochastic regime. The six panels show that the random ACT dynamics preserve a coherent large-scale phase-space organization, while at the same time displaying broadened recurrence patterns and nontrivial probability structure induced by noise.

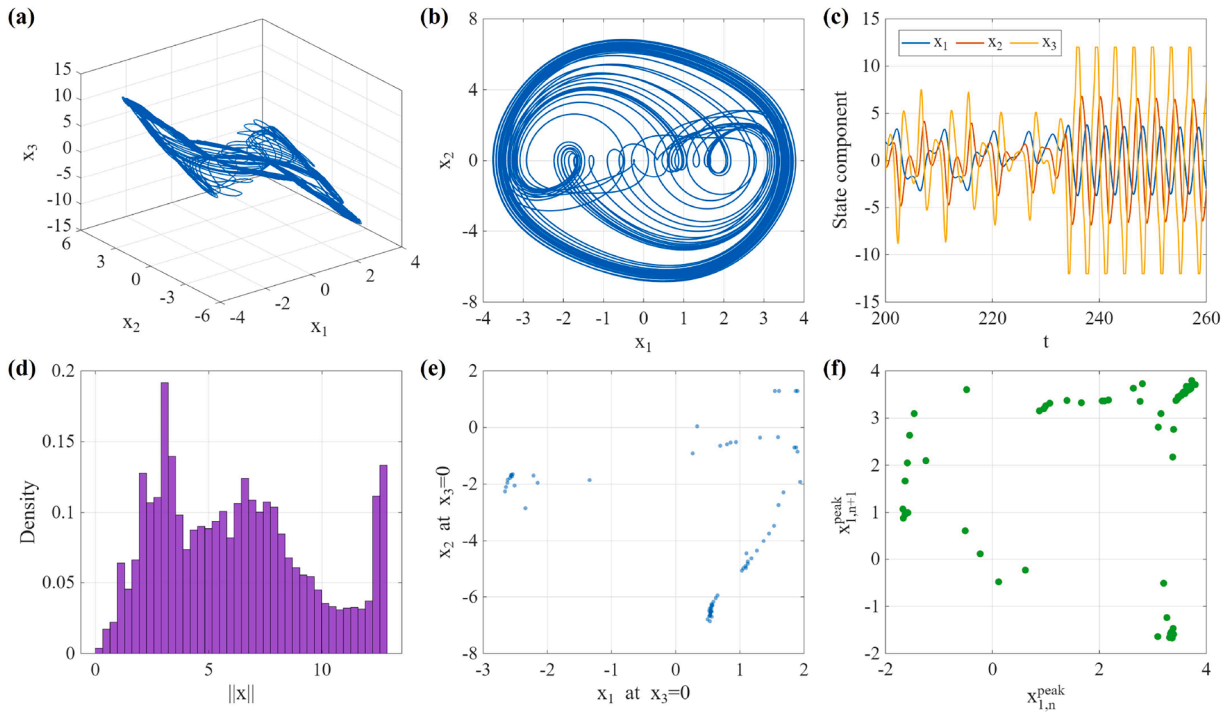

Fig. 4. Random-attractor diagnostics for the stochastic ACT dynamics: (a) 3D random ACT attractor at baseline noise; (b) projection of the random attractor on the $x_1 - x_2$ plane; (c) late-time stochastic evolution on the random attractor; (d) radial probability density on the random attractor; (e) Poincaré section of the random attractor; (f) peak-to-peak return map of the random attractor.

The three-dimensional portrait in the first panel shows that the stochastic orbit remains confined within a bounded elongated region whose global shape is still strongly reminiscent of the deterministic ACT attractor. This confirms that the deterministic spiral-reinjection skeleton continues to organize the long-time stochastic motion. The corresponding projection onto the x_1-x_2 plane further clarifies this point. The noisy trajectory fills a broader region than in the deterministic case, and the loops become visibly thicker, indicating that stochastic forcing expands the effective neighborhood explored by the orbit. Nevertheless, the overall two-lobed organization remains recognizable, which suggests that the random attractor is not an unstructured diffusion cloud but a geometrically meaningful stochastic extension of the deterministic attractor.

The late-time temporal evolution shown in the third panel provides additional insight into how noise modifies the attractor without destroying its oscillatory character. All three components remain bounded, but their amplitudes vary irregularly, and the larger bursts occur intermittently rather than periodically. In particular, the third component x_3 again shows the strongest excursions, which is consistent with the fact that the stochastic perturbation is injected directly into the third equation. This panel indicates that the noisy attractor supports persistent irregular oscillation rather than transient fluctuations around a single equilibrium region.

A particularly useful feature of Fig. 4 is the inclusion of the radial probability density of the state norm $\|\mathbf{x}\|$, where $\|\mathbf{x}\|$ denotes the Euclidean distance of the state from the origin. The histogram reveals that the random attractor is associated with a nonuniform radial distribution rather than a sharply concentrated shell. The density is spread over a relatively broad interval, which reflects the coexistence of compact spiral motion and larger stochastic excursions. This statistical view complements the geometric portraits by showing that the attractor has an internal distributional structure, not just a visible shape in phase space.

The last two panels further demonstrate that the return dynamics remain nontrivial under stochastic forcing. The Poincaré section, obtained from upward crossings of the plane $x_3 = 0$, still forms an organized point set, but the points are more scattered than in the deterministic baseline case. This is the expected signature of randomization of the return mechanism. Similarly, the peak-to-peak return map of successive local maxima of x_1 remains structured, but the points are more dispersed and occupy a broader region of the plane. This means that stochastic forcing perturbs the recurrence law while preserving an identifiable nonlinear return geometry.

Overall, Fig. 4 shows that the stochastic ACT system admits a well-defined random-attractor regime at the baseline noise intensity. The attractor remains bounded, geometrically organized, and statistically nontrivial. This result is important for the subsequent control analysis, because it confirms that the noisy ACT dynamics possess a coherent random phase-space structure that can serve as a meaningful target neighborhood for stochastic orbit steering.

6.2. *Baseline coupled FBSDE dynamics and control diagnostics*

Fig. 5 presents the core controlled results of the present study and illustrates how the coupled FBSDE framework performs stochastic orbit steering near the ACT attractor. The figure combines geometric comparison, ensemble statistics, tracking performance, control

behavior, and adjoint evolution under the baseline parameter setting. Taken together, these panels show that the proposed control law does not simply suppress the dynamics, but instead attempts to guide the stochastic trajectory toward a prescribed reference orbit while preserving the large-scale ACT phase-space structure.

The first panel compares the deterministic reference orbit with one controlled sample path in three-dimensional phase space. The controlled trajectory remains distributed around the same global spiral-chaotic region as the reference orbit, which indicates that the controller acts in an orbit-following manner rather than forcing the system toward an artificial equilibrium. At the same time, visible deviations remain, especially during larger excursions along the elongated branches of the attractor. This is consistent with the fact that the control problem is formulated in a stochastic setting, so exact pathwise coincidence is neither expected nor required. The relevant objective is instead the reduction of average deviation from the reference orbit.

This interpretation is reinforced by the second panel, where a controlled stochastic path is compared with an uncontrolled one under the same general dynamical regime. The uncontrolled path exhibits more pronounced deviation from the desired orbit geometry, whereas the controlled path remains more consistently aligned with the reference attractor region. The difference is not a complete geometric collapse, but a clear reduction in orbit drift. This is precisely the qualitative behavior sought in stochastic orbit steering. The controller regulates the noisy ACT motion while still allowing the trajectory to evolve within a nontrivial chaotic neighborhood.

The third panel compares the reference state components with the corresponding controlled ensemble means. Here, x_1^{ref}, x_2^{ref}, and x_3^{ref} denote the three components of the deterministic reference orbit, while the dashed curves represent the ensemble means of the controlled forward process. The agreement is not exact, especially for the third component, but the ensemble averages follow the broad oscillatory trend of the reference signal. This indicates that the control law is effective at the mean level, even though individual sample paths remain subject to significant stochastic distortion. In particular, the larger discrepancy in the third channel is dynamically understandable, since this channel carries both the nonlinear ACT activity and the direct stochastic forcing.

The fourth panel gives the evolution of the tracking error norm. The solid curve represents the mean tracking error, and the dashed curves indicate one standard deviation above and below that mean. The error remains bounded over the whole simulation horizon, but it increases gradually and shows several bursts at later times. This reveals an important aspect of the problem. Orbit steering near a stochastic chaotic attractor is feasible, but it becomes progressively more difficult over long horizons as diffusion accumulates and chaotic transport amplifies deviations. The relatively narrow gap between the mean curve and the surrounding bounds in much of the interval suggests that the ensemble dispersion of the tracking error remains reasonably controlled, even when the absolute error becomes larger.

The fifth panel shows the ensemble-mean control signal. The control remains moderate for most of the time horizon, with alternating positive and negative phases that reflect the oscillatory nature of the tracking objective. Larger corrections appear at later times, which is consistent with the growth of the tracking error observed in the previous panel. This behavior indicates that the controller responds adaptively to the evolving orbit mismatch instead of applying a uniformly strong forcing throughout the entire interval. Such a pattern is desirable in the present context, because excessive forcing would undermine the geometric character of the ACT motion.

Finally, the sixth panel presents the ensemble means of the backward components Y_1, Y_2, and Y_3, which form the adjoint state in the coupled FBSDE system. These quantities encode the backward propagation of future tracking cost through the nonlinear stochastic dynamics. Their oscillatory and strongly time-dependent behavior confirms that the control mechanism is genuinely coupled to the evolving ACT geometry rather than being generated by a static feedback rule. The relatively pronounced variation of Y_1 and Y_2, together with the nontrivial evolution of Y_3, indicates that the adjoint field captures both immediate mismatch and longer-horizon transport effects. Since the optimal control is determined by the third backward component, the figure also shows that orbit steering is mediated by a dynamically structured adjoint response rather than by a purely local correction.

Overall, Fig. 5 demonstrates that the coupled FBSDE control framework is capable of maintaining stochastic ACT trajectories in the neighborhood of a prescribed reference orbit while preserving the essential attractor geometry. The control improves orbit alignment relative to the uncontrolled case, the ensemble means retain the principal oscillatory pattern of the target trajectory, and the adjoint variables exhibit the expected nontrivial backward dynamics associated with a genuinely coupled stochastic optimal control problem.

Fig. 6 gives a more direct view of the internal dynamics of the coupled ACT-FBSDE system at both the pathwise and ensemble levels. In contrast to the previous figure, which emphasized reference tracking and control effectiveness, the present figure focuses on the structure of the forward state, the backward state, the martingale coefficients, and the iteration behavior of the coupled solver. Overall, the results show that the controlled ACT dynamics remain geometrically coherent, while the backward and stochastic components retain clear nonlinear and random features.

The first panel shows a representative forward ACT path in three-dimensional phase space. The trajectory still follows the characteristic elongated ACT geometry, indicating that the coupled control does not destroy the basic attractor structure. The second panel presents the backward-state portrait on the Y_1-Y_2 plane. Its broad and folded shape suggests that the adjoint dynamics are strongly nonlinear and evolve in a nontrivial way along the controlled orbit. The third panel displays the backward martingale coefficients Z_1, Z_2, and Z_3 for one sample path. These quantities fluctuate around zero for most of the interval, but intermittent bursts are visible, indicating localized stochastic sensitivity in the backward equation.

The fourth and fifth panels highlight pathwise variability and ensemble dispersion. The comparison of two forward paths shows that, although both trajectories share the same global oscillatory pattern, visible differences in amplitude and phase remain over time. This confirms that the control constrains the stochastic motion without eliminating randomness completely. The standard deviations of the forward components further show that dispersion grows with time, and that the third component has the largest variability.

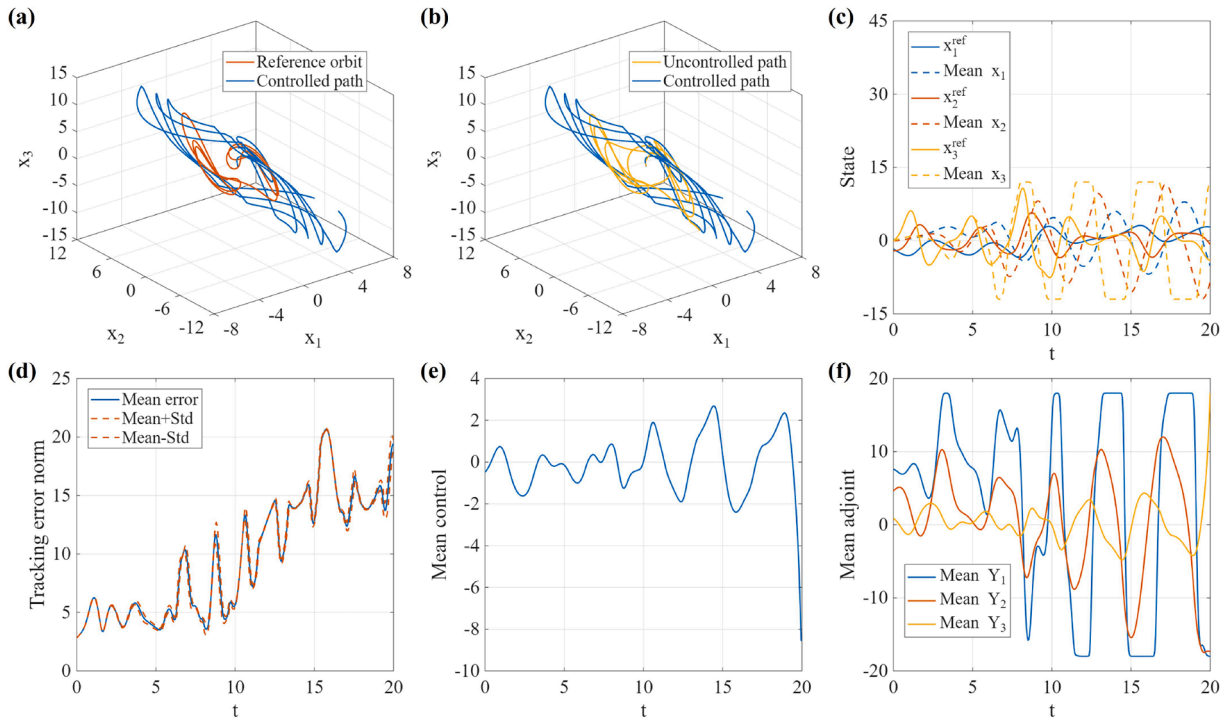

Fig. 5. Optimal orbit steering near the ACT attractor under coupled FBSDE control: (a) reference ACT orbit and one controlled sample path; (b) uncontrolled versus controlled stochastic ACT path; (c) reference states and controlled ensemble means; (d) tracking error evolution under optimal feedback; (e) ensemble-mean control signal; (f) ensemble means of backward components.

This is consistent with the fact that the third channel is the most active part of the ACT dynamics and is directly influenced by both noise and control.

The last panel shows the convergence history of the fully coupled iteration. The residual increases moderately across the Picard steps rather than decaying, which indicates that the coupled ACT-FBSDE problem remains numerically demanding. Nevertheless, the growth is gradual, not explosive, suggesting that the computation still stays within a controlled approximation regime. Overall, Fig. 6 confirms that the proposed framework captures not only the geometric behavior of the controlled ACT system, but also the nontrivial backward and stochastic structures that are intrinsic to a fully coupled FBSDE formulation.

Fig. 7 provides additional baseline diagnostics that further clarify the interaction between the controlled forward ACT dynamics and the associated adjoint variables. In contrast to the previous figures, which focused more strongly on global orbit steering and ensemble-level control performance, the present figure emphasizes local geometric relations, return behavior, terminal-error distribution, and correlation structure. These diagnostics reveal how the coupled state and adjoint components interact beyond standard tracking-error summaries.

The first panel shows the coupled portrait between $x_1(t)$ and $Y_3(t)$. This plot directly reflects the link between the forward dynamics and the third backward component, which is particularly important because Y_3 determines the optimal feedback through the control law. The portrait is clearly nonlinear and does not collapse onto a simple monotonic curve, indicating that the control action is generated through a nontrivial state-adjoint relationship rather than through a fixed proportional correction. The fourth panel, which gives the backward-state portrait on the $Y_1 - Y_3$ plane, supports the same conclusion. The adjoint trajectory occupies an extended and folded region, showing that the backward variables evolve in a strongly structured manner under the baseline control regime.

The second and third panels examine recurrence properties of one controlled path. The Poincaré section, formed from crossings of the plane $x_3 = 0$, produces an organized set of points rather than a diffuse cloud, which suggests that the controlled motion still preserves a coherent return structure in phase space. The peak-to-peak return map of successive local maxima of x_1 remains sparse but nonlinear, indicating that the controlled trajectory retains nontrivial oscillatory recurrence instead of becoming dynamically trivial. Together, these two panels show that the baseline control modifies the orbit without destroying its internal return geometry.

The last two panels provide statistical information. The histogram of terminal tracking error is concentrated in a relatively narrow interval, with most realizations clustering around the dominant central range rather than being widely spread. This suggests that, under baseline control, the terminal mismatch remains reasonably consistent across the ensemble. The final panel shows the time-resolved correlation between the observable $\psi(X_t)$ and $Y_3(t)$, where $\psi(X_t)$ denotes the scalar diagnostic observable constructed from the forward state. The correlation oscillates between positive and negative values over time, which indicates that the relation between forward orbit geometry and adjoint response is time-dependent and sign-changing rather than fixed. Overall, Fig. 7 shows that the baseline controlled ACT-FBSDE system possesses a coherent coupled structure at both the geometric and statistical levels, further supporting the effectiveness and internal consistency of the proposed framework.

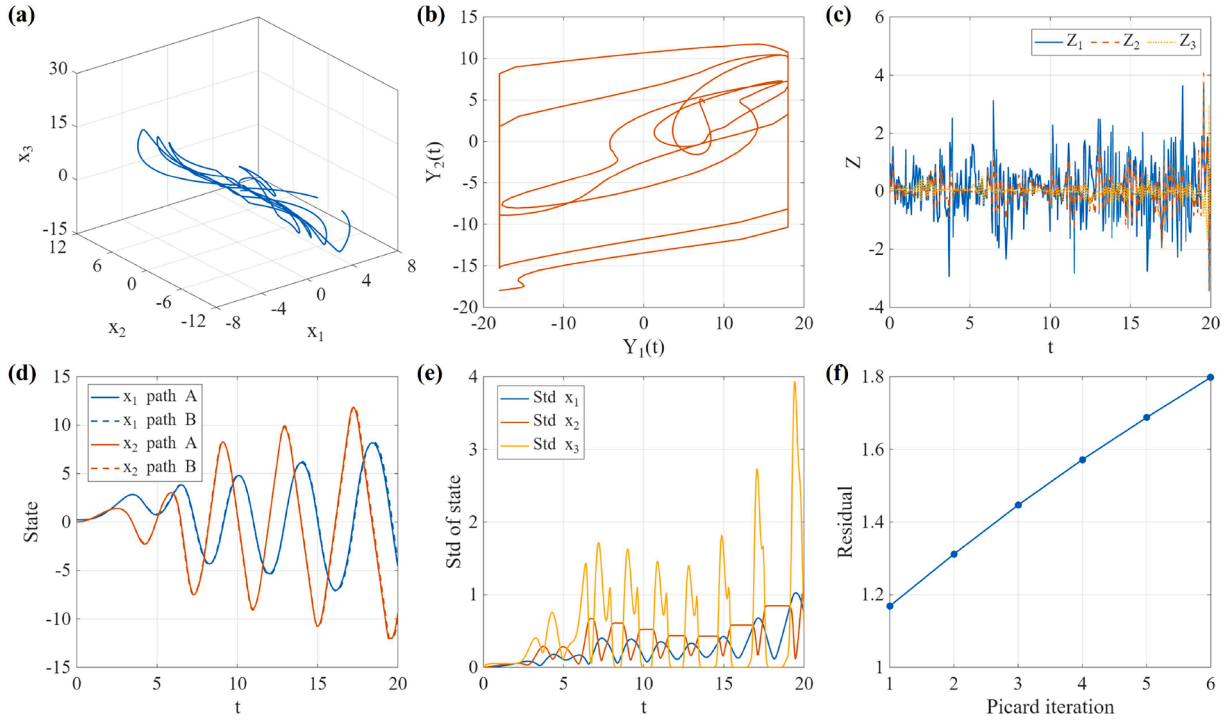

Fig. 6. Pathwise and ensemble diagnostics of the coupled ACT-FBSDE system: (a) representative forward ACT path; (b) backward-state portrait on the $Y_1 - Y_2$ plane; (c) backward martingale coefficients for one path; (d) two-path comparison of forward components; (e) ensemble dispersion of forward states; (f) convergence history of the fully coupled iteration.

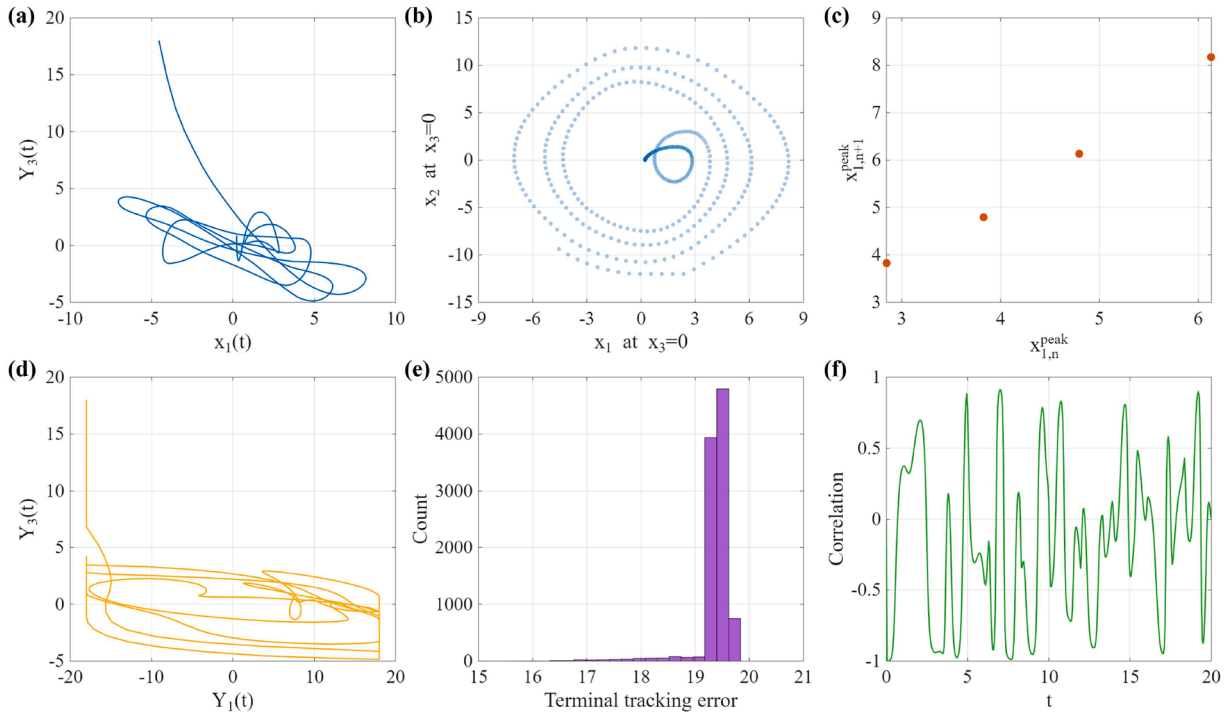

Fig. 7. Additional coupled-state and adjoint diagnostics under baseline control: (a) coupled portrait between x_1 and Y_3; (b) Poincaré section of one controlled path; (c) peak-to-peak return map for one controlled path; (d) backward-state portrait on the $Y_1 - Y_3$ plane; (e) distribution of terminal tracking error; (f) ensemble correlation between $\psi(X_t)$ and $Y_3(t)$.

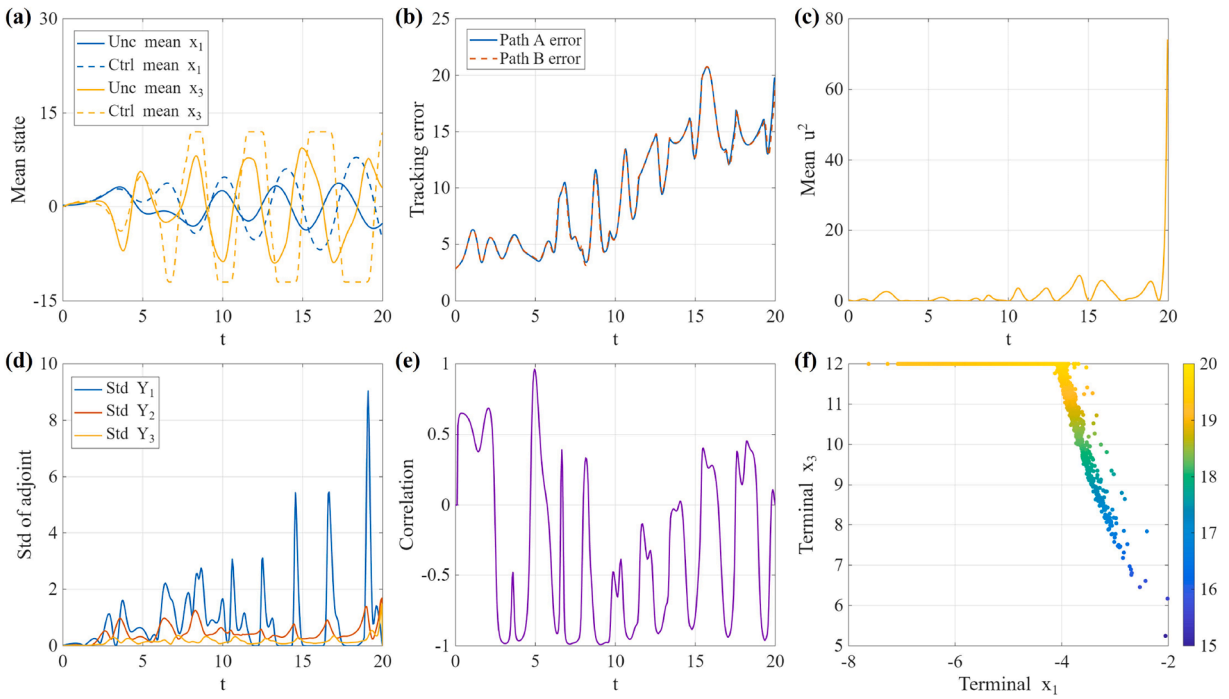

Fig. 8. Supplementary non-surface diagnostics for controlled and uncontrolled ACT dynamics: (a) controlled and uncontrolled ensemble means; (b) sample-path tracking errors; (c) time-resolved average control energy; (d) ensemble dispersion of backward variables; (e) ensemble correlation between x_1 and Y_3; (f) terminal-state cloud colored by terminal error.

Fig. 8 provides supplementary diagnostics that compare the controlled and uncontrolled ACT dynamics from both forward and backward perspectives. Unlike the previous figures, which focused either on attractor structure or on baseline controlled trajectories, the present figure highlights ensemble-level contrasts, pathwise tracking behavior, control-energy concentration, backward-state dispersion, and terminal-state distribution. These diagnostics reveal how the coupled FBSDE control reshapes the stochastic ACT dynamics beyond simple orbit plots.

The first panel compares the ensemble means of the uncontrolled and controlled dynamics for x_1 and x_3. The controlled means deviate visibly from the uncontrolled ones over most of the time interval, especially in the third component. This indicates that the control action has a persistent influence on the average orbit evolution rather than only producing occasional local corrections. The second panel shows the tracking errors of two representative sample paths. The two curves remain close to each other for most of the horizon, which suggests that the pathwise tracking performance is relatively consistent across different realizations, even though the error grows at later times.

The third panel presents the time-resolved average control energy, measured through the ensemble mean of u^2, where u denotes the control input. The curve remains moderate for much of the interval but develops several clear peaks, with a particularly strong increase near the terminal stage. This indicates that stronger control effort is required when the accumulated stochastic deviation becomes more difficult to correct. A related feature appears in the fourth panel, which shows the ensemble dispersion of the backward variables. The standard deviation of Y_1 is noticeably larger than those of Y_2 and Y_3, especially at several later-time peaks, implying that uncertainty in the adjoint field is distributed unevenly across its components.

The fifth panel gives the ensemble correlation between x_1 and Y_3. The correlation oscillates repeatedly between positive and negative values, showing that the coupling between the forward state and the control-relevant backward component is strongly time-dependent. This again supports the interpretation that the control mechanism is dynamically structured rather than static. Finally, the terminal state cloud in the (x_1, x_3) plane, colored by the terminal tracking error, shows that terminal realizations remain concentrated along a narrow band instead of spreading across a broad two-dimensional region. This suggests that, despite the presence of stochastic forcing, the controlled system preserves a relatively organized terminal-state structure, and that larger terminal errors are associated with specific regions of the terminal phase cloud rather than with complete loss of coherence. Overall, Fig. 8 further confirms that the proposed coupled control framework modifies the ACT dynamics in a systematic and geometrically meaningful way at both the ensemble and pathwise levels.

6.3. *Parameter sensitivity and response-surface analysis*

Fig. 9 summarizes how the performance of the ACT-FBSDE framework changes when the excitation parameter a and the noise intensity σ are varied simultaneously. The six response surfaces describe the running tracking error, terminal tracking error, control

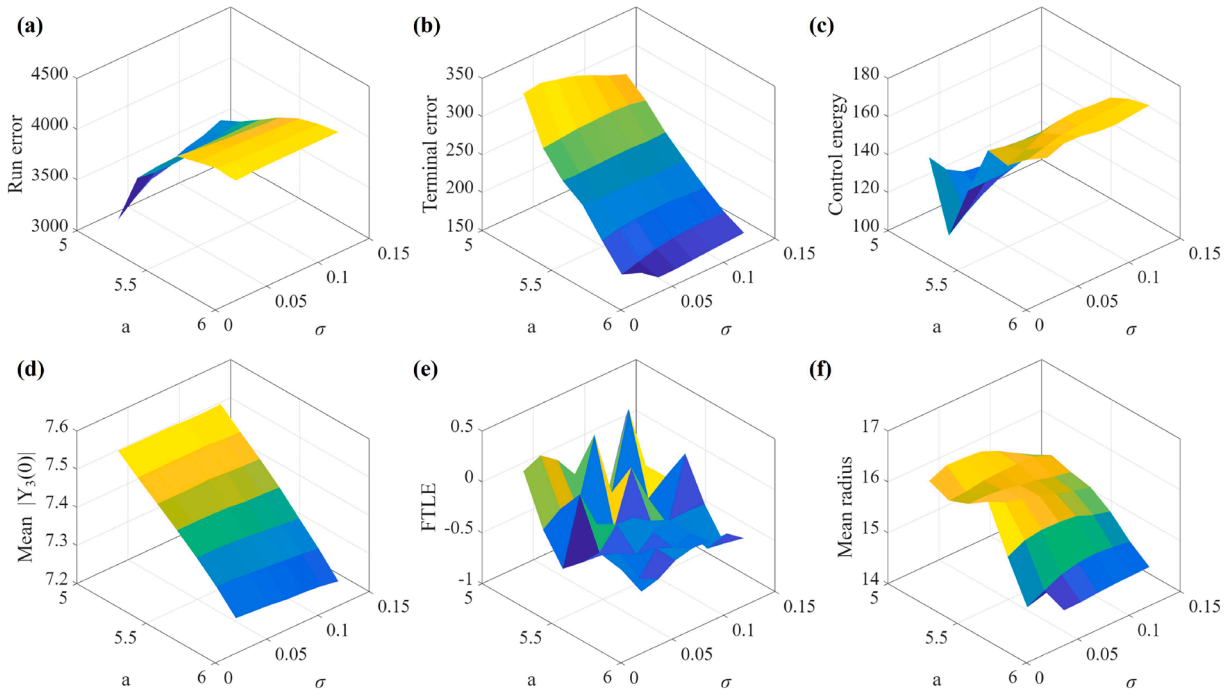

Fig. 9. Response surfaces on the a-σ plane for ACT-FBSDE performance: (a) running tracking error; (b) terminal tracking error; (c) control energy; (d) initial adjoint magnitude; (e) finite-time separation exponent; (f) mean orbit radius.

energy, mean initial adjoint magnitude, finite-time separation exponent, and mean orbit radius. Taken together, these surfaces show that the coupled control system is sensitive to both deterministic excitation and stochastic forcing, but that the influence of a is generally more systematic than that of σ in the displayed parameter window.

The first two panels indicate a clear contrast between running and terminal tracking behavior. The running tracking error remains at a relatively high level throughout the scanned region and varies smoothly with the parameters, with larger values appearing mainly as a increases. By contrast, the terminal tracking error shows a more pronounced downward trend as a moves toward the upper end of the interval. This suggests that stronger linear excitation does not necessarily improve the cumulative tracking performance over the whole time horizon, but it may still help reduce the final mismatch at the terminal time. In other words, the effect of a on control quality is not uniform across different performance measures.

The third and fourth panels show that the control energy and the mean magnitude of the initial adjoint component $|Y_3(0)|$ vary more moderately across the a-σ plane. The control-energy surface exhibits a structured but relatively smooth dependence, indicating that the energetic burden of control changes continuously rather than abruptly in this parameter region. The surface for the initial adjoint magnitude is even smoother, with only mild variation. This implies that the initial backward response of the coupled system remains comparatively stable under moderate joint perturbations of excitation and noise.

The fifth panel, showing the finite-time Lyapunov exponent (FTLE), is visibly more irregular than the other surfaces. Its alternating positive and negative regions indicate that short-horizon local separation is highly sensitive to parameter variation and does not follow the smoother patterns seen in the tracking or energy indicators. This means that local orbit sensitivity and global control performance should not be identified with one another. The last panel shows that the mean orbit radius remains within a relatively narrow range and changes more regularly than the FTLE surface, implying that the overall geometric scale of the controlled motion is preserved even when local separation properties fluctuate.

Overall, Fig. 9 shows that the coupled ACT-FBSDE performance is jointly shaped by deterministic excitation and stochastic forcing, but not all observables respond in the same manner. The response surfaces suggest that a mainly governs the large-scale geometric and tracking characteristics, whereas σ adds a secondary but still visible modulation through stochastic broadening. This result supports the view that parameter sensitivity in the present problem is multi-layered, with different performance indices emphasizing different aspects of the controlled chaotic dynamics.

Fig. 10 shows how the performance of the ACT-FBSDE framework changes when the parameter b and the control penalty coefficient r are varied jointly. Here, b is the linear coupling-damping parameter in the ACT drift, while r weights the control cost in the objective functional. Compared with the a-σ plane, the present parameter plane is more directly related to the balance between intrinsic system dissipation and control expenditure. The six response surfaces indicate that both parameters have a clear influence on tracking quality, but the effect of r is especially pronounced in several key metrics.

The first two panels show the running and terminal tracking errors. The running tracking error remains relatively large over most of the scanned region, but its surface is not monotonic and contains visible variations across the b-r plane. The terminal tracking

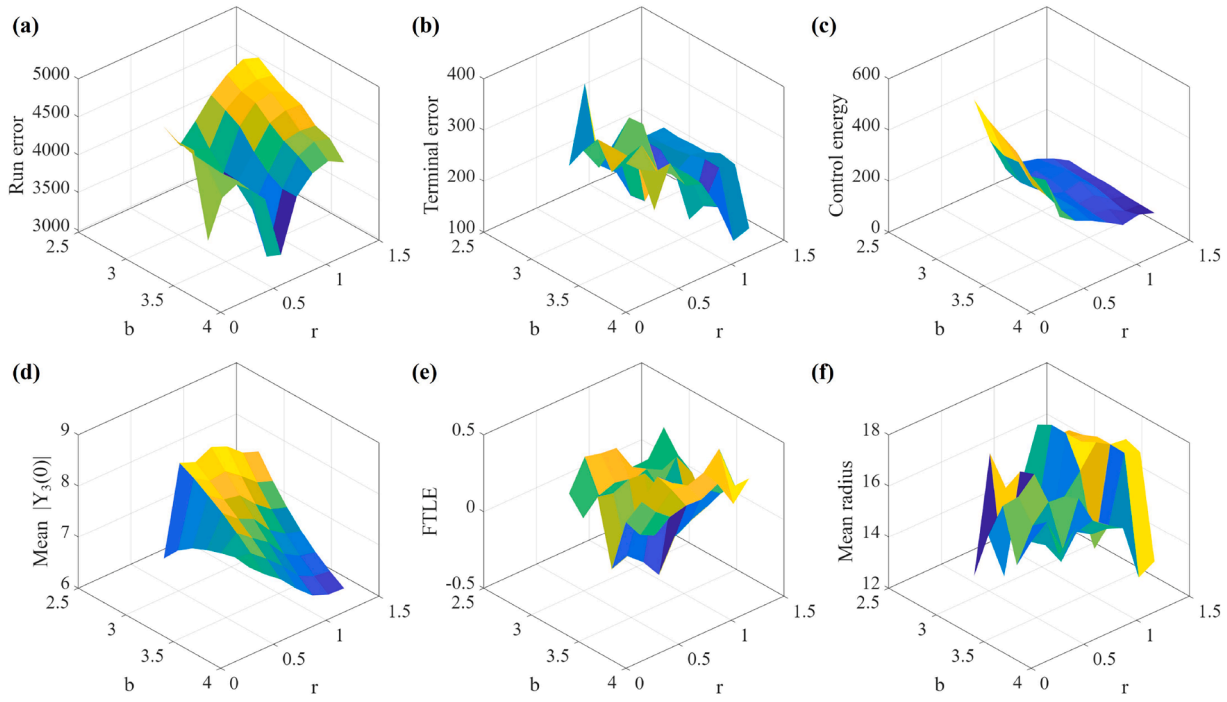

Fig. 10. Response surfaces on the *b*-*r* plane for ACT-FBSDE performance: (a) running tracking error; (b) terminal tracking error; (c) control energy; (d) initial adjoint magnitude; (e) finite-time separation exponent; (f) mean orbit radius.

error exhibits even stronger local variation, suggesting that final-time control quality is sensitive to the joint choice of damping and control penalty. In particular, smaller values of r, which correspond to weaker penalization of control effort, tend to be associated with improved terminal tracking in some regions, although this improvement is not uniform across the whole surface.

The third and fourth panels help clarify this trade-off. The control-energy surface decreases markedly as r increases, which is exactly what one would expect, since a larger control penalty suppresses the strength of the feedback action. At the same time, the surface for the mean initial adjoint magnitude $|Y_3(0)|$ also varies substantially, showing that the backward sensitivity of the control system changes together with the energetic cost structure. This indicates that the effect of r is not limited to reducing the size of the control, but also reshapes the internal adjoint response of the coupled FBSDE system.

The fifth and sixth panels concern the finite-time Lyapunov exponent and the mean orbit radius. As in the previous figure, the FTLE surface is less smooth than the tracking or energy surfaces, with alternating positive and negative regions. This again shows that local finite-time separation is more sensitive and less regular than the global performance indicators. By contrast, the mean orbit radius remains within a comparatively narrow range, even though some local variation is still visible. This suggests that the joint variation of b and r influences control quality and energetic burden more strongly than the overall spatial scale of the controlled orbit.

Overall, Fig. 10 indicates that the *b*-*r* plane captures a central compromise in the ACT-FBSDE framework. Increasing r reduces control expenditure, but this may weaken tracking performance, while variation in b modifies the background ACT dynamics and thereby changes the effectiveness of the same feedback mechanism. The figure therefore highlights that the coupled orbit-steering performance is shaped not only by excitation and noise, but also by the interplay between intrinsic damping and control cost.

Fig. 11 examines how the ACT-FBSDE performance changes when the running-state weights q_1 and q_3 are varied jointly. Here, q_1 and q_3 are the diagonal entries of the running weight tensor $\mathbf{Q}$ associated with the first and third state components, respectively. Since these two channels play different roles in the ACT dynamics, the figure is useful for clarifying how the weighting strategy in the objective functional reshapes tracking quality, control expenditure, and the internal adjoint response.

The first two panels show the running and terminal tracking errors. The running tracking error decreases as the weighting moves toward the larger-q_1, larger-q_3 region, which indicates that stronger penalization of state deviation improves cumulative orbit-following performance over the time horizon. The terminal tracking error, however, displays a less uniform surface and retains some local variation. This suggests that increasing the running-state weights improves the global tracking tendency more clearly than it improves final-time accuracy. In other words, the influence of $(q_1,\ q_3)$ is more systematic for the accumulated error than for the terminal mismatch.

The third and fourth panels reveal a clear cost-sensitivity trade-off. The control-energy surface rises markedly as q_3 increases and also grows with q_1 in much of the scanned region. This means that better state regulation is achieved at the expense of stronger control effort. The same trend is reflected in the surface for the mean initial adjoint magnitude $|Y_3(0)|$, which increases rather smoothly across

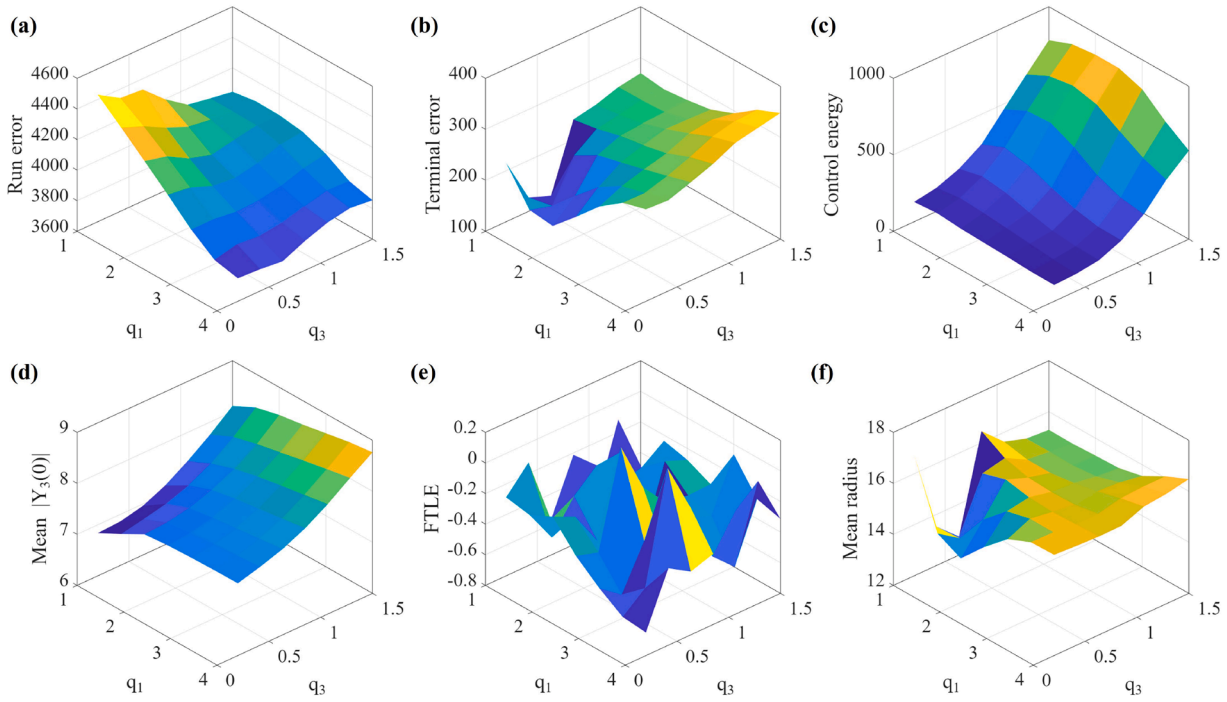

Fig. 11. Response surfaces on the q_1-q_3 plane for ACT-FBSDE performance: (a) running tracking error; (b) terminal tracking error; (c) control energy; (d) initial adjoint magnitude; (e) finite-time separation exponent; (f) mean orbit radius.

the plane. Since Y_3 is the backward component entering the feedback law, this shows that larger running-state weights strengthen the initial adjoint response and thereby intensify the control mechanism.

The fifth panel, corresponding to the finite-time Lyapunov exponent, is again much less regular than the other surfaces. Its fluctuating structure indicates that local finite-time sensitivity does not follow the same smooth trend as the tracking and energy indicators. By contrast, the last panel shows that the mean orbit radius remains within a relatively narrow band and varies more smoothly over the parameter plane. This implies that changing q_1 and q_3 alters the quality and energetic cost of orbit steering more strongly than it changes the overall spatial scale of the controlled motion.

Overall, Fig. 11 shows that the choice of running-state weights has a direct and meaningful effect on ACT-FBSDE performance. Larger values of q_1 and q_3 generally improve running tracking quality, but they also require more control energy and produce a stronger adjoint response. The figure therefore highlights a practical design trade-off: tighter orbit regulation can be achieved through stronger weighting of the forward-state error, but this comes with a clear increase in control burden.

7. Conclusion

This paper developed a fully coupled FBSDE framework for optimal orbit steering near an Arneodo-Coullet-Tresser (ACT) spiral attractor under stochastic perturbations. Instead of forcing the ACT system toward an equilibrium, the proposed formulation tracked a deterministic reference orbit segment extracted from the attractor itself, so that the intrinsic spiral geometry of the chaotic motion could be retained. On this basis, a stochastic optimal control problem was established, and the stochastic maximum principle led naturally to a nonlinear fully coupled forward-backward system in which the third backward component entered the active ACT channel through the optimal feedback law. The resulting model provided a coherent connection between stochastic chaotic dynamics, orbit tracking, and adjoint-based control.

The analytical part of the study clarified the structure of the model through a Hamiltonian formulation, a variational derivation, a local solvability discussion, and a decoupling-field interpretation. The numerical results further showed that the ACT attractor maintains a recognizable deterministic and stochastic geometric skeleton, while the coupled FBSDE control can guide noisy trajectories toward the reference orbit without collapsing the dynamics into a trivial state. The baseline simulations demonstrated meaningful improvements in orbit alignment relative to the uncontrolled case, and the additional diagnostics confirmed that the forward dynamics, backward adjoint variables, and stochastic sensitivity remain strongly coupled throughout the evolution. The response-surface results also showed that model parameters, control penalization, and tracking weights influence performance in different ways, with tracking accuracy, control energy, and local orbit sensitivity exhibiting distinct parameter dependence.

Overall, the present work suggests that coupled FBSDEs provide a useful and comparatively underexplored framework for studying stochastic orbit steering in spiral chaotic systems. The ACT setting highlights that effective control in a noisy chaotic environment

need not rely on equilibrium suppression, but can instead be formulated as geometry-preserving trajectory regulation near a nontrivial attractor. Future work may extend this framework to longer horizons, higher-dimensional chaotic systems, more robust numerical schemes for strongly coupled iterations, and alternative cost structures adapted to random attractor neighborhoods.

CRediT authorship contribution statement

Dong Feng: Writing – review & editing, Writing – original draft, Visualization, Validation, Software, Resources, Project administration, Methodology, Investigation, Funding acquisition, Formal analysis, Data curation, Conceptualization.

Data availability

Data will be made available on request.

Declaration of competing interest

The authors declare that they have no known competing financial interests or personal relationships that could have appeared to influence the work reported in this paper.

Acknowledgement

This research is supported by the China Scholarship Council (CSC., No. 202308080042).

References

[1] Rahaman MM, Bhowmick S, Mondal RN, Saha SC. A computational study of chaotic flow and heat transfer within a trapezoidal cavity. Energies 2023;16(13):5031. https://doi.org/10.3390/en16135031
[2] del Castillo-Negrete D. Self-consistent chaotic transport in fluids and plasmas. Chaos 2000;10(1):75–88. https://doi.org/10.1063/1.166477
[3] Ipatovs A, Victor IC, Pikulins D, Tjukovs S, Litvinenko A. Complete bifurcation analysis of the vilnius chaotic oscillator. Electronics 2023;12(13):2861. https://doi.org/10.3390/electronics12132861
[4] Ngamsa Tegnitsap JV, Fotsin HB, Megam Ngouonkadi EB. Magnetic coupling based control of a chaotic circuit: case of the van der pol oscillator coupled to a linear circuit. Chaos Solit Fractals 2021;152:111319. https://doi.org/10.1016/j.chaos.2021.111319
[5] Feng D. A compactor-soil coupling model considering mechanical inertia and its delayed feedback active suspension control. Int J Non-Linear Mech 2025;179:105245. https://doi.org/10.1016/j.ijnonlinmec.2025.105245
[6] Feng D. A novel four-degree-of-freedom compactor–soil coupling model. Nonlinear Dyn 2026;114(8). https://doi.org/10.1007/s11071-026-12419-6
[7] Moon FC, Shaw SW. Chaotic vibrations of a beam with non-linear boundary conditions. Int J Non-Linear Mech 1983;18(6):465–77. https://doi.org/10.1016/0020-7462(83)90033-1
[8] Mehri S, Scheutzow M, Stannat W, Zangeneh BZ. Propagation of chaos for stochastic spatially structured neuronal networks with delay driven by jump diffusions. Ann Appl Probab 2020;30(1):175–207. https://doi.org/10.1214/19-AAP1499
[9] Jhangeer A, Abdelkader A. Multistability, chaos, and control in the deterministic and stochastic dynamics of noise-driven nonlinear oscillators. Entropy 2026;28(2):214. https://doi.org/10.3390/e28020214
[10] Feng D. Explosive synchronization induced by temporal higher-order interactions in activity-driven simplicial complexes. Phys Lett A 2026;586:131707. https://doi.org/10.1016/j.physleta.2026.131707
[11] Dykman GI, Landa PS, Neymark YI. Synchronizing the chaotic oscillations by external force. Chaos Solit Fractals 1991;1(4):339–53. https://doi.org/10.1016/0960-0779(91)90025-5
[12] Fotsin HB, Daafouz J. Adaptive synchronization of uncertain chaotic colpitts oscillators based on parameter identification. Phys Lett A 2005;339(3–5):304–15. https://doi.org/10.1016/j.physleta.2005.03.049
[13] Konishi K, Generating chaotic behavior in an oscillator driven by periodic forces. Phys Lett A 2003;320(2-3):200–6. https://doi.org/10.1016/j.physleta.2003.11.024
[14] Feng D, Fu C, Liu PA. A modified johnson-kendall-roberts contact model for pavement engineering: consideration of time-dependent surface energy. Powder Technol 2026;468:121701. https://doi.org/10.1016/j.powtec.2025.121701
[15] Feng D. A DEM-based particle–force chain informatics framework for data-driven evaluation of pavement pre-compaction. Adv Eng Inform 2026;71:104402. https://doi.org/10.1016/j.aei.2026.104402
[16] Catsis S, Hall CL, Jeffrey MR. The hidden sensitivity of non-smooth dynamics. Phys D Nonlinear Phenom 2024;463:134165. https://doi.org/10.1016/j.physd.2024.134165
[17] Sarkar P, Ray DS. Nonlinear stochastic differential equations: a renormalization group approach to direct calculation of moments. Phys Rev E 2024;110(6-1):64217. https://doi.org/10.1103/PhysRevE.110.064217
[18] Varghese V, Saha N. Investigation of stochastic nonlinear dynamics of ocean engineering systems through path integration. Phys D Nonlinear Phenom 2020;402:132227. https://doi.org/10.1016/j.physd.2019.132227
[19] Varzaneh M, Riedel S. A dynamical theory for singular stochastic delay differential equations II: nonlinear equations and invariant manifolds. DCDS-B 2021;26(8):4587–612. https://doi.org/10.3934/dcdsb.2020304
[20] Abdelwahed HG, Elbaz IM, Sohaly MA, Abdelrahman M AE, Alsarhan AF, Al-rasheed AM. Exploring nonlinear chaotic systems with applications in stochastic processes. Sci Rep 2024;14(1):30608. https://doi.org/10.1038/s41598-024-82057-8
[21] Faranda D, Sato Y, Saint-Michel B, Wiertel C, Padilla V, Dubrulle B, et al. Stochastic chaos in a turbulent swirling flow. Phys Rev Lett 2017;119(1):014502. https://doi.org/10.1103/PhysRevLett.119.014502
[22] Zak M. Stochastic representation of chaos using terminal attractors. Chaos Solit Fractals 2005;24(3):863–8. https://doi.org/10.1016/j.chaos.2004.09.098
[23] Arneodo A, Coullet P, Tresser C. Occurence of strange attractors in three-dimensional volterra equations. Phys Lett A 1980;79(4):259–63. https://doi.org/10.1016/0375-9601(80)90342-4
[24] Arneodo A, Coullet P, Tresser C. Possible new strange attractors with spiral structure. Commun Math Phys 1981;79(4):573–9. https://doi.org/10.1007/BF01209312
[25] Brandstater A, Swinney HL. Strange attractors in weakly turbulent couette-taylor flow. Phys Rev Gen Phys 1987;35(5):2207–20. https://doi.org/10.1103/PhysRevA.35.2207
[26] Chen Z, Zhao H. Self-similar attractor sets of the lorenz model in parameter space. Chaos Solit Fractals 2023;173:113651. https://doi.org/10.1016/j.chaos.2023.113651

[27] Lorenz EN. Deterministic nonperiodic flow. J Atmos Sci 1963;20(2):130–41. https://doi.org/10.1175/1520-0469(1963)020<0130:DNF>2.0.CO;2
[28] Afraimovich V, Chow S-N, Liu W. Lorenz type attractors from codimension one bifurcation. J Dyn Diff Equat 1995;7(2):375–407. https://doi.org/10.1007/BF02219362
[29] Argoul F, Arneodo A, Richetti P. A three-dimensional dissipative map modeling type-II intermittency. J Phys Fr 1988;49(5):767–75. https://doi.org/10.1051/jphys:01988004905076700
[30] El Karoui N, Peng S, Quenez M-C. Backward stochastic differential equations in finance. Math Finance 1997;7(1):1–71. https://doi.org/10.1111/1467-9965.00022
[31] Pardoux E, Peng S. Adapted solution of a backward stochastic differential equation. Syst Control Lett 1990;14(1):55–61. https://doi.org/10.1016/0167-6911(90)90082-6
[32] Wang G, Wu Z, Xiong J. An introduction to optimal control of FBSDE with incomplete information. Cham: Springer International Publishing; 2018.
[33] Bandini E, Confortola F, Cosso A. BSDE representation and randomized dynamic programming principle for stochastic control problems of infinite-dimensional jump-diffusions. Electron J Probab 2019;24:1–37. https://doi.org/10.1214/19-EJP333
[34] Pagès G, Sagna A. Improved error bounds for quantization based numerical schemes for BSDE and nonlinear filtering. Stoch Process Appl 2018;128(3):847–83. https://doi.org/10.1016/j.spa.2017.05.009
[35] Klimsiak T, Rzymowski M. Nonlinear BSDEs on a general filtration with drivers depending on the martingale part of the solution. Stoch Process Appl 2023;161:424–50. https://doi.org/10.1016/j.spa.2023.04.011
[36] Kobylanski M. Backward stochastic differential equations and partial differential equations with quadratic growth. Ann Probab 2000;28(2):558–602. https://doi.org/10.1214/aop/1019160253
[37] Du K, Chen S. Backward stochastic partial differential equations with quadratic growth. J Math Anal Appl 2014;419(1):447–68. https://doi.org/10.1016/j.jmaa.2014.04.050
[38] Feng D. Dissipative cascaded multistep backward stochastic differential equation (BSDE) with polynomial growth. Commun Nonlinear Sci Numer Simul 2026;110066. https://doi.org/10.1016/j.cnsns.2026.110066
[39] Ceci C, Cretarola A, Russo F. BSDEs under partial information and financial applications. Stoch Process Appl 2014;124(8):2628–53. https://doi.org/10.1016/j.spa.2014.03.003
[40] Øksendal B, Sulem A. Portfolio optimization under model uncertainty and BSDE games. Quant Finance 2011;11(11):1665–74. https://doi.org/10.1080/14697688.2011.615219
[41] Feng D. A quadratic BSDE framework for risk-adjusted noise-induced switching in bistable nonlinear oscillators under stochastic volatility. Chaos Solit Fractals 2026;207:118021. https://doi.org/10.1016/j.chaos.2026.118021
[42] Geiss C, Labart C. Simulation of BSDEs with jumps by Wiener Chaos expansion. Stoch Process Appl 2016;126(7):2123–62. https://doi.org/10.1016/j.spa.2016.01.006
[43] Shi Y, Zhu P. Synchronization of stochastic competitive neural networks with different timescales and reaction-diffusion terms. Neural Comput 2014;26(9):2005–24. https://doi.org/10.1162/NECO_a_00629
[44] Guo G. Finite difference methods for the BSDEs in finance. Int J Financ Stud 2018;6(1):26. https://doi.org/10.3390/ijfs6010026
[45] Djehiche B, Dumitrescu R, Zeng J. A propagation of chaos result for weakly interacting nonlinear snell envelopes. Stoch Process Appl 2025;188:104669. https://doi.org/10.1016/j.spa.2025.104669
[46] Morel J-M, Takens F, Teissier B, Ma J, Yong J. Forward-backward stochastic differential equations and their applications. Berlin, Heidelberg: Springer Berlin Heidelberg; 2007.
[47] Hamadene S, Lepeltier J. Backward equations, stochastic control and zero-sum stochastic differential games. Stoch Stoch Rep 1995;54(3-4):221–31. https://doi.org/10.1080/17442509508834006
[48] Archibald R, Bao F. Kernel learning backward sde filter for data assimilation. J Comput Phys 2022;455:111009. https://doi.org/10.1016/j.jcp.2022.111009
[49] Itô K. On a formula concerning stochastic differentials. Nagoya Math J 1951;3:55–65. https://doi.org/10.1017/S0027763000012216
[50] Kloeden PE, Platen E. Numerical solution of stochastic differential equations. Berlin, New York: Springer; 3rd ed.; 1999.